Comput. Methods Appl. Mech. Engrg. 247–248 (2012) 179–200

Contents lists available at SciVerse ScienceDirect

Comput. Methods Appl. Mech. Engrg.

journal homepage: www.elsevier.com/locate/cma

On imposing dynamic contact-angle boundary conditions for wall-bounded liquid–gas flows

S. Dong

Center for Computational & Applied Mathematics, Department of Mathematics, Purdue University, United States

ARTICLE INFO

Article history:
Received 19 May 2012
Received in revised form 27 July 2012
Accepted 31 July 2012
Available online 18 August 2012

Keywords:
Contact line
Contact angle
Phase field approach
Two phase flow
Large density ratio

ABSTRACT

We present an efficient scheme within the phase field framework for imposing dynamic contact angle boundary conditions for wall-bounded flows of two immiscible incompressible fluids with large density ratios. First, we develop an algorithm for imposing the dynamic contact angle boundary conditions to the Cahn–Hilliard equation. Our algorithm consists of two components: (i) we ignore the boundary conditions and transform the Cahn–Hilliard equation into two *nominally de-coupled* Helmholtz type equations; (ii) we treat the dynamic contact angle boundary conditions in such a manner that the two Helmholtz-type equations are *truly de-coupled*. Then, we combine this algorithm, together with a scheme for variable-density Navier–Stokes equations we developed recently, to form an efficient method for the coupled system of Navier–Stokes and Cahn–Hilliard equations for contact line problems involving large density ratios. The overall method can deal with moving contact lines under dynamic and also static contact angle boundary conditions. It is endowed with several attractive features that make the method very efficient. In particular, computations for all flow variables are completely decoupled. The resultant linear algebraic systems after discretization for all flow variables involve only constant and time-independent coefficient matrices, which can be pre-computed during pre-processing, even though the coupled Navier–Stokes/Cahn–Hilliard system involves variable density and variable viscosity. Ample numerical simulations of wall-bounded air/water two-phase flows have been presented to demonstrate the capability of the method for dealing with contact line problems under dynamic and static contact-angle conditions involving large density ratios.

1. Introduction

When the mixture of two immiscible fluids is in contact with a solid wall, a moving contact line forms where the fluid interface intersects the wall. Moving contact line problems are omnipresent in natural world and man-made applications, wherever one fluid displaces another on a solid surface. Numerical simulations of such problems are complicated by a non-physical divergent stress at the contact line [14], which stems from the fact that continuum fluid mechanics breaks down at molecular distances from the contact line. Several models/approaches have been proposed to circumvent this difficulty in the context of continuum mechanics, including precursor film [7], slip [20,18], and diffuse interface or phase field formulations [21]. We consider the phase field approach in the current paper.

Methods for dealing with the contact angle (static/dynamic), i.e. the angle formed between the fluid interface and the solid wall, in numerical simulations have emerged only recently and are an active area of research. The approaches chosen largely depend on the numerical strategies used for the interface description (such as level set [27,31], front tracking [36,35], volume of fluids [30], or phase field [25,24]) and the methods for spatial discretization (e.g. finite difference- or finite element-based). They can be based on contact-angle models or contact-angle laws [5,19], see e.g. [1,13] with volume of fluids, [26] with front tracking, and [34] with level set methods for this type of strategies. They can also be based on geometric formulations, which is usually implemented with finite difference-type methods, see e.g. [8,23] for this type of strategies. Contact angle conditions can also be enforced in the weak sense, which is usually implemented with finite element-type methods, see e.g. [44,41].

Hereafter we focus on the phase field approach for contact line problems. In this approach, the sharp fluid interface is replaced by a thin smooth transition layer (i.e. diffuse interface) connecting the two immiscible incompressible fluids, and the two-phase system is described by a phase field function, which varies continuously within the transition layer and is mostly uniform in the bulk phases. The governing equations consist of the incompressible Navier–Stokes equations with an extra term which arises naturally from a variational procedure and accounts for the surface tension effect [24], and the Cahn–Hilliard equation which describes the evolution of the phase field function. With the phase field

E-mail address: sdong@math.purdue.edu

0045-7825/$ - see front matter © 2012 Elsevier B.V. All rights reserved.
http://dx.doi.org/10.1016/j.cma.2012.07.023

approach, the contact line moves naturally on the solid surface due to a diffusive flux across the interface driven by the gradient of the chemical potential [21,41], and there is no longer a singularity.

The contact angle boundary condition for the phase field function arises from the consideration of wall energy, which accounts for the effect of fluid–solid interfacial tensions. Consider the free energy of a system of two immiscible fluids given by the form

$$\mathcal{F} = \int_\Omega \left[\frac{\lambda}{2}\nabla\phi\cdot\nabla\phi + \frac{\lambda}{4\eta^2}\left(\phi^2-1\right)^2\right]d\Omega + \int_{\partial\Omega} f_w(\phi)dA, \tag{1}$$

where Ω is the flow domain, ϕ is the phase field function ($\phi=\pm1$ represent the fluid bulks and $\phi=0$ marks the fluid/fluid interface), and λ and η are respectively the mixing energy density and the capillary width. The first integral in the above equation represents the mixing energy. The second integral represents the wall energy due to the fluid–solid interfacial tension, where $f_w(\phi)$ is the fluid–solid interfacial tension function defined on the wall.

To determine the form of $f_w(\phi)$, the following requirements/assumptions seem reasonable: (1) f_w takes the values of fluid one-solid interfacial tension (σ_{w1}) and fluid two-solid interfacial tension (σ_{w2}) in the wall regions of the two bulk fluids, i.e. $f_w(\phi=\pm1)=\sigma_{w1}$ and σ_{w2}; (2) f_w takes the average value of σ_{w1} and σ_{w2} at the fluid interface, i.e. $f_w(\phi=0)=(\sigma_{w1}+\sigma_{w2})/2$; (3) f_w' vanishes in the wall regions of the two bulk fluids, i.e. $f_w'(\phi=\pm1)=0$; (4) the Young's equation holds with the contact angle on the wall, $\sigma_{w2}-\sigma_{w1}=\sigma\cos\theta_s$, where σ is the fluid–fluid surface tension and θ_s is the static contact angle between the fluid interface and the wall measured on the side of the first fluid. The simplest polynomial function that satisfies these requirements, obtained by Hermite interpolation, is given by

$$f_w(\phi) = \sigma\cos\theta_s\frac{\phi(\phi^2-3)}{4} + \frac{1}{2}(\sigma_{w1}+\sigma_{w2}). \tag{2}$$

The form of $f_w(\phi)$ in Eq. (2) was first given by [21], see also [41].

With the help of a variational procedure on (1), one can come up with a boundary condition for the phase field function like the following,

$$\mathbf{n}\cdot\nabla\phi = -\frac{1}{\lambda}f_w'(\phi), \quad \text{on } \partial\Omega, \tag{3}$$

where $\mathbf{n}$ is the outward-pointing unit vector normal to the wall, and $f_w'(\phi)=-\frac{3}{4}\sigma\cos\theta_s(1-\phi^2)$. Note that the boundary condition (3) and (2) imply that, when the fluid interface intersects the wall, it will be at local equilibrium and the contact angle assumes the equilibrium (static) contact angle. That is, there will be no relaxation of the dynamic contact angle to the equilibrium angle. The majority of phase field simulations for contact line problems so far have employed the static contact angle condition (3), see [21,42,8,44,41,15].

To allow for the relaxation of dynamic contact angle and non-equilibrium, Jacqmin [21] suggests the following form of boundary condition on the phase field function,

$$-D_w\left(\frac{\partial\phi}{\partial t}+\mathbf{u}\cdot\nabla\phi\right) = \mathbf{n}\cdot\nabla\phi + \frac{1}{\lambda}f_w'(\phi), \quad \text{on } \partial\Omega, \tag{4}$$

where $\mathbf{u}$ is the velocity, and D_w is a phenomenological parameter which we will refer to as the dynamic wall mobility. The above condition is reduced to Eq. (3) for $D_w=0$. This condition in a similar form has also been obtained through a variational approach in [28].

Very few studies exist in the phase field literature that have taken into account the effects of dynamic contact angle through the boundary condition (4). To the best of the author's knowledge, Yue and Feng [38] and Carlson et al. [4,3] are the only ones that have used some simplified variants of (4) in simulations. In [38], Yue and Feng ignored the time derivative term on the left hand side of Eq. (4) by assuming a steady slow flow. On the other hand, Carlson et al. [4,3] ignored the convective term on the left hand of (4) in their simulations.

In this paper, we will develop algorithms for efficient numerical treatment of the dynamic contact angle boundary condition (4), together with the no flux condition of the chemical potential, in the context of coupled Navier–Stokes and Cahn–Hilliard equations involving large density ratios. We will first present an efficient algorithm for imposing the condition (4) to the Cahn–Hilliard equation. The key property of our algorithm is that, the 4th order Cahn–Hilliard equation, together with the dynamic contact angle boundary condition (4), will be formulated as two *de-coupled* Helmholtz type equations after discretization. In contrast, a usual formulation would result in coupled equations after discretization, inducing significantly larger computational cost. Then, we will combine the above algorithm, and a scheme for variable-density Navier–Stokes equations we developed recently [12], to form an efficient method for the coupled system of Navier–Stokes and Cahn–Hilliard equations involving large density ratios. The overall method takes into account the effects of dynamic and also static contact angles, and moreover possesses several properties that make the algorithm very efficient. In particular, only constant and time-independent coefficient matrices, which can be pre-computed, are involved for all flow variables (velocity, pressure, and phase field function) after discretization, even though the coupled Navier–Stokes/Cahn–Hilliard system involves variable density and variable viscosity. In addition, the method is suitable for two-phase flows with large density ratios, which will be demonstrated with numerical simulations of a number of air–water flows involving solid walls of various hydrophobicities.

The novelty of the presented algorithm lies in the numerical treatment of the dynamic contact angle boundary conditions, which enables the re-formulation of the Cahn–Hilliard problem (Cahn–Hilliard equation plus dynamic contact-angle boundary conditions) into solving two *de-coupled* Helmholtz type equations. We also would like to emphasize the importance of the use of a *discrete* zero-flux boundary condition for the chemical potential in the current method, rather than the *continuous* zero-flux condition. The use of the continuous zero-flux condition for the chemical potential results in catastrophic loss of mass for one of the fluid phases in numerical simulations. On the other hand, the strategies for dealing with variable-density Navier–Stokes equations and for combining Cahn–Hilliard equation and variable-density Navier–Stokes equations derive largely from our previous work [12].

We employ the spectral element approach [22,11,9] for spatial discretization of the governing equations in the current paper, because of its high-order accuracy and geometric flexibility [43,10]. The presented algorithms are formulated and implemented with C^0 spectral elements, and the formulations without change also apply to low-order finite elements. The presented strategies for the numerical treatment of the dynamic contact-angle boundary conditions are however general, not limited by the particular spatial discretization schemes.

1.1. Coupled Navier–Stokes/Cahn–Hilliard equations

To provide a context for the algorithmic developments in subsequent sections, let us briefly summarize here the set of governing equations for a two-phase system with the phase field approach. We consider a mixture of two immiscible, incompressible fluids contained in the flow domain Ω. Let ρ_1 and ρ_2 respectively denote the densities of the two fluids, and μ_1 and μ_2 denote their dynamic viscosities. This two-phase system is described by the following coupled system of equations:

$$\rho\left(\frac{\partial \mathbf{u}}{\partial t}+\mathbf{u}\cdot\nabla\mathbf{u}\right)=-\nabla p+\nabla\cdot\left[\mu(\nabla\mathbf{u}+\nabla\mathbf{u}^T)\right]-\lambda\nabla\cdot(\nabla\phi\nabla\phi)+\mathbf{f}(\mathbf{x},t), \tag{5a}$$

$$\nabla\cdot\mathbf{u}=0, \tag{5b}$$

$$\frac{\partial\phi}{\partial t}+\mathbf{u}\cdot\nabla\phi=-\lambda\gamma_1\nabla^2\left[\nabla^2\phi-h(\phi)\right]+g(\mathbf{x},t). \tag{5c}$$

In the above equations, $\mathbf{u}(\mathbf{x},t)$ is velocity, $p(\mathbf{x},t)$ is pressure, and $\mathbf{f}(\mathbf{x},t)$ is a body force (such as gravity), where t is time and $\mathbf{x}$ is the spatial coordinate. $\phi(\mathbf{x},t)$ denotes the phase field function, $-1\leqslant\phi\leqslant 1$. The flow regions with $\phi=1$ and $\phi=-1$ respectively represent the first and the second fluids. $h(\phi)$ is the derivative of the second term in the mixing energy integral in Eq. (1), given by $h(\phi)=\frac{1}{\eta^2}\phi(\phi^2-1)$. λ is the mixing energy density, and is related to the surface tension σ by $\lambda=\frac{3}{2\sqrt{2}}\sigma\eta$ [39], where σ is assumed to be constant. γ_1 is the mobility of the interface, and is assumed to be constant in this paper. The density, ρ, and the dynamic viscosity, μ, are related to the phase field function by,

$$\rho(\phi)=\frac{\rho_1+\rho_2}{2}+\frac{\rho_1-\rho_2}{2}\phi,\quad \mu(\phi)=\frac{\mu_1+\mu_2}{2}+\frac{\mu_1-\mu_2}{2}\phi. \tag{6}$$

Consequently, both the density and the dynamic viscosity in Eq. (5a) are time-dependent field variables. $g(\mathbf{x},t)$ in Eq. (5c) is a given source term, and $g(\mathbf{x},t)=0$ in practical simulations. The superscript in $(\cdot)^T$ denotes the transpose of $(\cdot)$.

Among the above set of equations, (5a) is the Navier–Stokes equation, involving a variable density and a variable dynamic viscosity, in which the term $\lambda\nabla\cdot(\nabla\phi\nabla\phi)$ represents the surface tension effect. Eq. (5c) (without the prescribed source term g) is the Cahn–Hilliard equation. This coupled system of equations are to be supplemented with appropriate boundary and initial conditions, to be discussed in subsequent sections.

2. Algorithms for imposing dynamic contact angle boundary conditions

2.1. Algorithm for Cahn–Hilliard equation with dynamic contact-angle boundary conditions

Let us consider how to solve the Cahn–Hilliard Eq. (5c), in which the velocity $\mathbf{u}(\mathbf{x},t)$ is assumed to be known, together with the following boundary conditions:

$$\mathbf{n}\cdot\nabla\left[\nabla^2\phi-h(\phi)\right]=g_c(\mathbf{x},t),\quad \text{on } \partial\Omega, \tag{7a}$$

$$-D_w\left(\frac{\partial\phi}{\partial t}+\mathbf{u}\cdot\nabla\phi\right)=\mathbf{n}\cdot\nabla\phi+\frac{1}{\lambda}f_w'(\phi)+g_b(\mathbf{x},t),\quad \text{on } \partial\Omega, \tag{7b}$$

where we require that $D_w\geqslant 0$. $g_c(\mathbf{x},t)$ and $g_b(\mathbf{x},t)$ are prescribed scalar field functions on domain boundary $\partial\Omega$. These functions, together with the source term $g(\mathbf{x},t)$ in (5c), enable the numerical tests in Section 3 for the convergence rates of the developed algorithms using an analytic solution together with the dynamic contact angle boundary conditions. If $g_c=0$, Eq. (7a) corresponds to the zero-flux condition of the chemical potential $G=\lambda\left[-\nabla^2\phi+h(\phi)\right]$ on $\partial\Omega$. If $g_b=0$, Eq. (7b) is reduced to the dynamic contact angle boundary condition (4). We will set $g_c=0$ and $g_b=0$ in practical simulations.

The Cahn–Hilliard Eq. (5c) and the boundary condition (7a) involve spatial orders higher than two, which cannot be handled readily with C^0 spectral elements. To impose the dynamic contact-angle boundary conditions and also to circumvent the difficulty with C^0 spectral elements, we will take the following strategy: (1) we will transform the semi-discretized Cahn–Hilliard equation into two *nominally de-coupled* Helmholtz type equations by ignoring the boundary conditions; (2) we will treat the dynamic contact-angle boundary conditions in such a manner that the two Helmholtz type equations are *truly de-coupled*. The weak forms of the overall algorithm can be directly employed in spectral element (or finite element) spatial discretizations.

2.1.1. Decomposition of Cahn–Hilliard equation into nominally de-coupled Helmholtz equations

Let χ denote a generic variable, and χ^n denote χ at time step n. Given $(\phi^n,\mathbf{u}^n)$, we first ignore the boundary conditions and discretize the Cahn–Hilliard equation (5c) in time as follows,

$$\frac{\gamma_0\phi^{n+1}-\hat{\phi}}{\Delta t}+\mathbf{u}^{*,n+1}\cdot\nabla\phi^{*,n+1}=-\lambda\gamma_1\nabla^2\left[\nabla^2\phi^{n+1}-\frac{S}{\eta^2}\left(\phi^{n+1}-\phi^{*,n+1}\right)-h(\phi^{*,n+1})\right]+g^{n+1}. \tag{8}$$

In the above equation, Δt is the time step size, and S is a chosen constant that satisfies a condition to be discussed below. If χ is a generic variable, then $\hat{\chi}$ in the above equation is defined by $\hat{\chi}=\sum_{k=0}^{J-1}\alpha_k\chi^{n-k}$, where J denotes the temporal order of accuracy ($J=1$ or 2), such that $\frac{1}{\Delta t}(\gamma_0\chi^{n+1}-\hat{\chi})$ represents the J-th order backward differentiation formula (BDF) of $\frac{\partial\chi}{\partial t}\big|^{n+1}$. $\chi^{*,n+1}$ represents a J-th order explicit approximation of χ^{n+1}, and is defined by $\chi^{*,n+1}=\sum_{k=0}^{J-1}\beta_k\chi^{n-k}$. More specifically,

$$\gamma_0\chi^{n+1}-\hat{\chi}=\begin{cases}\chi^{n+1}-\chi^n, & \text{if } J=1,\\ \frac{3}{2}\chi^{n+1}-2\chi^n+\frac{1}{2}\chi^{n-1}, & \text{if } J=2,\end{cases}$$
$$\chi^{*,n+1}=\begin{cases}\chi^n, & \text{if } J=1,\\ 2\chi^n-\chi^{n-1}, & \text{if } J=2.\end{cases} \tag{9}$$

The semi-discretized Cahn–Hilliard equation (8) can be written as

$$\nabla^2\left[\nabla^2\phi^{n+1}-\frac{S}{\eta^2}\phi^{n+1}\right]+\frac{\gamma_0}{\lambda\gamma_1\Delta t}\phi^{n+1}=Q \tag{10}$$

where $Q=\frac{1}{\lambda\gamma_1}\left(g^{n+1}-\mathbf{u}^{*,n+1}\cdot\nabla\phi^{*,n+1}+\frac{\hat{\phi}}{\Delta t}\right)+\nabla^2\left[h(\phi^{*,n+1})-\frac{S}{\eta^2}\phi^{*,n+1}\right]$.

Now we would like to transform (10) into two *de-coupled* Helmholtz type equations if not considering the boundary conditions. Let $\Phi^{n+1}=\nabla^2\phi^{n+1}-\frac{S}{\eta^2}\phi^{n+1}$. Then Eq. (10) can be written as a system of two coupled second-order equations as follows,

$$\begin{bmatrix}\nabla^2\Phi^{n+1}\\ \nabla^2\phi^{n+1}\end{bmatrix}+\mathbf{A}\begin{bmatrix}\Phi^{n+1}\\ \phi^{n+1}\end{bmatrix}=\begin{bmatrix}Q\\ 0\end{bmatrix}, \tag{11}$$

where $\mathbf{A}$ is a 2×2 constant matrix given by

$$\mathbf{A}=\begin{bmatrix}0 & \frac{\gamma_0}{\lambda\gamma_1\Delta t}\\ -1 & -\frac{S}{\eta^2}\end{bmatrix}.$$

For stability we impose the requirement that all the eigen-values of matrix $\mathbf{A}$ be real and non-positive numbers. This leads to the following condition,

$$\frac{S}{\eta^2}\geqslant\sqrt{\frac{4\gamma_0}{\lambda\gamma_1\Delta t}}, \tag{12}$$

which the chosen constant S must satisfy. Consequently, the two eigen-values of $\mathbf{A}$ are given by

$$\begin{cases}\xi_1=-\frac{S}{2\eta^2}\left(1-\sqrt{1-\frac{4\gamma_0}{\lambda\gamma_1\Delta t}\frac{\eta^4}{S^2}}\right),\\ \xi_2=-\frac{S}{2\eta^2}\left(1+\sqrt{1-\frac{4\gamma_0}{\lambda\gamma_1\Delta t}\frac{\eta^4}{S^2}}\right).\end{cases} \tag{13}$$

Let $\mathbf{J}$ denote the canonical Jordan form of $\mathbf{A}$, and let $\mathbf{P}$ denote the non-singular matrix comprised of the eigen-vectors or generalized

eigen-vectors of $\mathbf{A}$ such that $\mathbf{P}^{-1}\mathbf{A}\mathbf{P}=\mathbf{J}$. Then Eq. (11) is transformed to

$$\mathbf{P}^{-1}\begin{bmatrix}\nabla^2\Phi^{n+1}\\ \nabla^2\phi^{n+1}\end{bmatrix}+\mathbf{J}\mathbf{P}^{-1}\begin{bmatrix}\Phi^{n+1}\\ \phi^{n+1}\end{bmatrix}=\mathbf{P}^{-1}\begin{bmatrix}Q\\ 0\end{bmatrix}. \tag{14}$$

There exist two possibilities: $\xi_1\neq\xi_2$ (or $S>\eta^2\sqrt{\frac{4\gamma_0}{\lambda\gamma_1\Delta t}}$), and $\xi_1=\xi_2$ (or $S=\eta^2\sqrt{\frac{4\gamma_0}{\lambda\gamma_1\Delta t}}$). For the first case $\xi_1\neq\xi_2$, we have

$$\mathbf{J}=\begin{bmatrix}\xi_1 & 0\\ 0 & \xi_2\end{bmatrix},\quad \mathbf{P}=\begin{bmatrix}\xi_2 & \xi_1\\ 1 & 1\end{bmatrix}. \tag{15}$$

Consequently, the matrix Eq. (14) is transformed into the following two *de-coupled* scalar Helmholtz equations,

$$\nabla^2\Psi_1^{n+1}+\xi_1\Psi_1^{n+1}=Q, \tag{16a}$$

$$\nabla^2\Psi_2^{n+1}+\xi_2\Psi_2^{n+1}=Q, \tag{16b}$$

where

$$\Psi_1^{n+1}=\Phi^{n+1}-\xi_1\phi^{n+1},\quad \Psi_2^{n+1}=\Phi^{n+1}-\xi_2\phi^{n+1}. \tag{17}$$

Therefore, the original semi-discretized Cahn–Hilliard equation (10) is equivalent to the formulation of two de-coupled Helmholtz equations, (16a) and (16b), about Ψ_1^{n+1} and Ψ_2^{n+1}.

Let us consider some variants of the formulation denoted by Eqs. (16a) and (16b). Subtract (16b) from (16a), and we obtain

$$\nabla^2\phi^{n+1}+(\xi_1+\xi_2)\phi^{n+1}=\Phi^{n+1}. \tag{18}$$

Therefore, we have the following variant formulations

$$\begin{cases}\nabla^2\Psi_1^{n+1}+\xi_1\Psi_1^{n+1}=Q,\\ \nabla^2\phi^{n+1}+\xi_2\phi^{n+1}=\Psi_1^{n+1},\end{cases} \tag{19}$$

and

$$\begin{cases}\nabla^2\Psi_2^{n+1}+\xi_2\Psi_2^{n+1}=Q,\\ \nabla^2\phi^{n+1}+\xi_1\phi^{n+1}=\Psi_2^{n+1},\end{cases} \tag{20}$$

where we have used (18) and (17) in the derivation. Note that in both of these variant formulations we can solve the two equations in an un-coupled manner, by first computing Ψ_1^{n+1} or Ψ_2^{n+1} and then ϕ^{n+1}.

For the case $\xi_1=\xi_2=\zeta=-\frac{S}{2\eta^2}$, we have

$$\mathbf{J}=\begin{bmatrix}\zeta & 1\\ 0 & \zeta\end{bmatrix},\quad \mathbf{P}=\begin{bmatrix}\zeta & -1\\ 1 & 0\end{bmatrix}. \tag{21}$$

Consequently, the matrix Eq. (14) is transformed into the following scalar Helmholtz equations

$$\begin{cases}\nabla^2\Psi_3^{n+1}+\zeta\Psi_3^{n+1}=Q,\\ \nabla^2\phi^{n+1}+\zeta\phi^{n+1}=\Psi_3^{n+1},\end{cases} \tag{22}$$

where $\Psi_3^{n+1}=\Phi^{n+1}-\zeta\phi^{n+1}$. Note that the two equations in (22) can be solved successively in an *un-coupled* manner.

Therefore, the semi-discretized Cahn–Hilliard Eq. (10) can be re-formulated as two *de-coupled* scalar Helmholtz type equations in several ways: (i) as Eqs. (16a) and (16b), (ii) as Eq. (19), (iii) as Eq. (20), or (iv) as Eq. (22). In any case, the computations of the two Helmholtz equations are nominally de-coupled. The de-coupling is considered only nominal because we have so far ignored the boundary conditions. If the boundary conditions are provided in an appropriate form, the two Helmholtz equations will be truly de-coupled. Otherwise, coupling will occur between the two equations through the boundary conditions.

Noting the similarity in forms among (19), (20) and (22), we re-write them as follows,

$$\nabla^2\psi^{n+1}-\left(\alpha+\frac{S}{\eta^2}\right)\psi^{n+1}=Q, \tag{23a}$$

$$\nabla^2\phi^{n+1}+\alpha\phi^{n+1}=\psi^{n+1}, \tag{23b}$$

where $\alpha=\xi_1$ or $\alpha=\xi_2$ given by Eq. (13), and S is a chosen constant satisfying (12). Note that the formulation represented by (23a) and (23b) can be used for both $\xi_1\neq\xi_2$ and $\xi_1=\xi_2$.

The form of the nominally de-coupled Helmholtz equations (23a) and (23b) with $\alpha=\xi_1=-\frac{S}{2\eta^2}\left(1-\sqrt{1-\frac{4\gamma_0}{\lambda\gamma_1\Delta t}\frac{\eta^4}{S^2}}\right)$ was first given by [39]. Our discussions above show that, besides this form, the semi-discretized Cahn–Hilliard equation (10) can also be formulated into de-coupled Helmholtz equations in other forms, for example, as Eqs. (16a) and (16b), or as Eqs. (23a) and (23b) with $\alpha=\xi_2$.

We note that the de-coupled Helmholtz equations (23a) and (23b) can be readily handled with C^0 spectral elements (or finite elements) after appropriate weak forms are obtained. We will use (23a) and (23b) in subsequent discussions.

2.1.2. Discretization of Boundary Conditions

Let us now consider the boundary conditions. Our goal is to treat the boundary conditions (7a)–(7b) in such a manner that Eqs. (23a) and (23b) can indeed be solved in a de-coupled fashion.

Consider first the condition (7a) for the chemical potential. We discretize this condition in time as follows

$$\mathbf{n}\cdot\nabla\left[\nabla^2\phi^{n+1}-\frac{S}{\eta^2}(\phi^{n+1}-\phi^{*,n+1})-h(\phi^{*,n+1})\right]=g_c^{n+1},\ \text{ on }\partial\Omega, \tag{24}$$

where g_c^{n+1} denotes $g_c(\mathbf{x},t)$ at time step $(n+1)$. The additional term, $\frac{S}{\eta^2}(\phi^{n+1}-\phi^{*,n+1})$, in the above discrete condition will not modify the overall temporal accuracy of the scheme because $\phi^{*,n+1}$ is a Jth order approximation of ϕ^{n+1}. But it is critical to the conservation of mass in light of the discretization of the Cahn–Hilliard equation in (8). Without this term in the discrete condition, catastrophic loss of mass for one of the phases of the fluids has been observed in numerical simulations.

Taking into account Eqs. (23b) and (24), we have the following boundary condition for ψ^{n+1},

$$\begin{aligned}\mathbf{n}\cdot\nabla\psi^{n+1}=&\left(\alpha+\frac{S}{\eta^2}\right)\mathbf{n}\cdot\nabla\phi^{n+1}\\ &+\mathbf{n}\cdot\nabla\left[h(\phi^{*,n+1})-\frac{S}{\eta^2}\phi^{*,n+1}\right]+g_c^{n+1},\ \text{ on }\partial\Omega.\end{aligned} \tag{25}$$

Using this boundary condition, we obtain the weak form of Eq. (23a) about ψ^{n+1},

$$\begin{aligned}&\int_\Omega\nabla\psi^{n+1}\cdot\nabla\varphi+\left(\alpha+\frac{S}{\eta^2}\right)\int_\Omega\psi^{n+1}\varphi\\ &=-\int_\Omega\frac{1}{\lambda\gamma_1}\left[g^{n+1}-\mathbf{u}^{*,n+1}\cdot\nabla\phi^{*,n+1}+\frac{\hat{\phi}}{\Delta t}\right]\varphi\\ &\quad+\int_\Omega\nabla\left[h(\phi^{*,n+1})-\frac{S}{\eta^2}\phi^{*,n+1}\right]\cdot\nabla\varphi+\int_{\partial\Omega}g_c^{n+1}\varphi\\ &\quad+\left(\alpha+\frac{S}{\eta^2}\right)\int_{\partial\Omega}\mathbf{n}\cdot\nabla\phi^{n+1}\varphi,\quad\forall\varphi\in H^1(\Omega),\end{aligned} \tag{26}$$

where φ is the test function, and we have eliminated the ∇^2 operator in Q of Eq. (23a) with integration by part. The weak form for Eq. (23b) about ϕ^{n+1} reads

$$\begin{aligned}\int_\Omega\nabla\phi^{n+1}\cdot\nabla\varphi-\alpha\int_\Omega\phi^{n+1}\varphi=&-\int_\Omega\psi^{n+1}\varphi+\int_{\partial\Omega}\mathbf{n}\cdot\nabla\phi^{n+1}\varphi,\\ &\forall\varphi\in H^1(\Omega).\end{aligned} \tag{27}$$

One can note that the equations for ψ^{n+1} and ϕ^{n+1}, (26) and (27), are fully coupled with each other because of the surface integral term involving $\mathbf{n}\cdot\nabla\phi^{n+1}$.

Now let us consider the dynamic contact-angle boundary condition (7b). We will treat this boundary condition in two different ways, respectively for the two Eqs. (26) and (27), in order to de-couple the computations for ψ^{n+1} and ϕ^{n+1}. For Eq. (26), we discretize (7b) as follows by treating $\frac{\partial\phi}{\partial t}$ explicitly,

$$-D_w\left(\left.\frac{\partial\phi}{\partial t}\right|^{*,n+1} + \mathbf{u}^{*,n+1}\cdot\nabla\phi^{*,n+1}\right) = \mathbf{n}\cdot\nabla\phi^{n+1} + \frac{1}{\lambda}f_w'(\phi^{*,n+1}) + g_b^{n+1}, \quad \text{on } \partial\Omega, \tag{28}$$

where g_b^{n+1} denotes $g_b(\mathbf{x},t)$ at time step $(n+1)$, and $\left.\frac{\partial\phi}{\partial t}\right|^{*,n+1}$ is an explicit approximation of $\frac{\partial\phi}{\partial t}$ at time step $(n+1)$ given by

$$\left.\frac{\partial\phi}{\partial t}\right|^{*,n+1} = \begin{cases} \frac{1}{\Delta t}(\phi^n - \phi^{n-1}), & \text{if } J=1,\\ \frac{1}{\Delta t}\left(\frac{5}{2}\phi^n - 4\phi^{n-1} + \frac{3}{2}\phi^{n-2}\right), & \text{if } J=2. \end{cases} \tag{29}$$

For Eq. (27), we treat $\frac{\partial\phi}{\partial t}$ implicitly and discretize (7b) as follows,

$$-D_w\left(\frac{\gamma_0\phi^{n+1}-\hat{\phi}}{\Delta t} + \mathbf{u}^{*,n+1}\cdot\nabla\phi^{*,n+1}\right) = \mathbf{n}\cdot\nabla\phi^{n+1} + \frac{1}{\lambda}f_w'(\phi^{*,n+1}) + g_b^{n+1}, \quad \text{on } \partial\Omega, \tag{30}$$

where $(\gamma_0\phi^{n+1}-\hat{\phi})$ is defined in (9).

Consequently, the weak form (26) for ψ^{n+1} is transformed into

$$\begin{aligned}\int_\Omega \nabla\psi^{n+1}\cdot\nabla\varphi + \left(\alpha+\frac{S}{\eta^2}\right)\int_\Omega \psi^{n+1}\varphi &= -\int_\Omega \frac{1}{\lambda\gamma_1}\left[g^{n+1} - \mathbf{u}^{*,n+1}\cdot\nabla\phi^{*,n+1} + \frac{\hat{\phi}}{\Delta t}\right]\varphi\\ &+ \int_\Omega \nabla\left[h(\phi^{*,n+1}) - \frac{S}{\eta^2}\phi^{*,n+1}\right]\cdot\nabla\varphi + \int_{\partial\Omega} g_c^{n+1}\varphi\\ &- \left(\alpha+\frac{S}{\eta^2}\right)\int_{\partial\Omega}\left[D_w\left(\left.\frac{\partial\phi}{\partial t}\right|^{*,n+1} + \mathbf{u}^{*,n+1}\cdot\nabla\phi^{*,n+1}\right)\right.\\ &\left.+ \frac{1}{\lambda}f_w'(\phi^{*,n+1}) + g_b^{n+1}\right]\varphi, \quad \forall\varphi\in H^1(\Omega),\end{aligned} \tag{31}$$

where we have used (28) to obtain an explicit approximation for $\mathbf{n}\cdot\nabla\phi^{n+1}$. In light of (30), the weak form (27) for ϕ^{n+1} is transformed into

$$\begin{aligned}\int_\Omega \nabla\phi^{n+1}\cdot\nabla\varphi - \alpha\int_\Omega\phi^{n+1}\varphi + \frac{\gamma_0 D_w}{\Delta t}\int_{\partial\Omega}\phi^{n+1}\varphi &= -\int_\Omega\psi^{n+1}\varphi + \int_{\partial\Omega}\left[-\frac{1}{\lambda}f_w'(\phi^{*,n+1}) + \frac{D_w}{\Delta t}\hat{\phi}\right.\\ &\left.- D_w\mathbf{u}^{*,n+1}\cdot\nabla\phi^{*,n+1} - g_b^{n+1}\right]\varphi, \quad \forall\varphi\in H^1(\Omega).\end{aligned} \tag{32}$$

One can observe that the computations for ψ^{n+1} and ϕ^{n+1} are now truly de-coupled, by successively solving the two Eqs. (31) and (32). One further notes that both (31) and (32) give rise to symmetric coefficient matrices after spatial discretization, and that these coefficient matrices are constant matrices and can be pre-computed during pre-processing. The weak forms (31) and (32) can be directly employed in C^0 spectral element (and also finite element) spatial discretizations.

Let us briefly comment on other possibilities for treating (7b). It is very tempting to use (28), by explicit treatment of $\frac{\partial\phi}{\partial t}$, for both weak forms (26) and (27), which will also de-couple the computations for ψ^{n+1} and ϕ^{n+1}. We have implemented this variant scheme, and from numerical tests we observe that, however, it is stable only for very small D_w values (typically $D_w \lesssim 0.002$), which is too small to exhibit any noticeable dynamic effect on the contact angle. It is unstable for larger D_w values. So this variant scheme cannot handle dynamic contact angles. Alternatively, one can also use (30) (implicit treatment of $\frac{\partial\phi}{\partial t}$) for both (26) and (27). However, this will couple up the computations for ψ^{n+1} and ϕ^{n+1}, inducing a higher computational cost. In contrast, the scheme we have introduced for treating the dynamic contact-angle boundary condition separately for ψ^{n+1} and ϕ^{n+1}, (28) and (30), is stable for large D_w values and simultaneously de-couples the computations for ψ^{n+1} and ϕ^{n+1}. These points will be demonstrated with numerical tests in Section 3.

In summary, given $(\phi^n, \mathbf{u}^n)$, the final procedure for computing ϕ^{n+1} from the Cahn–Hilliard equation, together with the dynamic contact-angle boundary conditions (7a) and (7b), is as follows: (i) solve Eq. (31) for ψ^{n+1}, and (ii) then solve Eq. (32) for ϕ^{n+1}.

2.2. Algorithm for coupled Navier–Stokes/Cahn–Hilliard equations with dynamic contact-angle boundary conditions

We will now combine the algorithm developed in the previous subsection, for the Cahn–Hilliard equation and dynamic contact-angle boundary conditions, with a scheme for the variable-density Navier–Stokes equations we developed in [12], to form an efficient method for the coupled system of Navier–Stokes/Cahn–Hilliard equations for contact-line problems involving large density ratios.

Consider the coupled Navier–Stokes/Cahn–Hilliard equations, (5a)–(5c), together with the dynamic contact-angle boundary conditions for the phase field function, (7a) and (7b), and the Dirichlet boundary condition for the velocity, (47) (in Appendix A). We will first de-couple the solution of the Cahn–Hilliard equation for the phase field function from that of the variable-density Navier–Stokes equations for the pressure/velocity, by treating explicitly the convective term in the Cahn–Hilliard Eq. (5c) and in the dynamic contact-angle boundary condition (7b). Then we employ the algorithm from Section 2.1 to solve the Cahn–Hilliard equation, together with the dynamic contact-angle boundary conditions, for the phase field function, and we employ a scheme for the variable-density Navier–Stokes equations we developed recently in [12] to solve for the pressure and velocity. For the sake of completeness, in Appendix A we have summarized the scheme for the variable-density Navier–Stokes equations from [12].

We first transform the Navier–Stokes equation (5a) into an equivalent form (48), by introducing an effective pressure $P = p + \frac{\lambda}{2}\nabla\phi\cdot\nabla\phi$. The governing equations now consist of (48), (5b) and (5c), supplemented by the boundary conditions (7a), (7b) and (47). We will develop algorithms for this system.

Specifically, given $(\mathbf{u}^n, P^n, \phi^n)$, we successively compute the phase field function ϕ^{n+1}, the pressure P^{n+1} and the velocity $\mathbf{u}^{n+1}$ with the following formulation:

(i) Solve (8) together with (24), (28) and (30) for ϕ^{n+1}.
(ii) Compute ρ^{n+1} and μ^{n+1} based on ϕ^{n+1}.
(iii) Solve (49a)–(49c) and (50a) and (50b) for P^{n+1} and $\mathbf{u}^{n+1}$ (Appendix A).

The algorithm for (i) has been developed in Section 2.1, and the algorithm for (iii) is summarized in Appendix A and detailed in [12]. For computing ρ^{n+1} and μ^{n+1} in (ii), we will employ Eq. (6), but with an exception for very large (or very small) density ratios ρ_2/ρ_1 (or ρ_1/ρ_2). For large density ratios (typically beyond $\sim 10^2$) we define an auxiliary variable $\tilde{\phi}$,

$$\tilde{\phi} = \begin{cases}\phi, & \text{if } |\phi|\leqslant 1,\\ \text{sign}(\phi), & \text{if } |\phi|>1\end{cases} \tag{33}$$

and compute density/viscosity based on $\tilde{\phi}$,

$$\rho = \frac{\rho_1+\rho_2}{2} + \frac{\rho_1-\rho_2}{2}\tilde{\phi}, \qquad \mu = \frac{\mu_1+\mu_2}{2} + \frac{\mu_1-\mu_2}{2}\tilde{\phi}. \tag{34}$$

The reason for using (34) for large density ratios has been discussed in [12]. It is related to the interplay between mass conservation and energy minimization inherent in the Cahn–Hilliard dynamics, which tends to induce a slight shift in the values of the phase field function in the bulk phases [40]. This may cause the numerically-computed phase field function to go slightly out of range $[-1,1]$ (by e.g. 10^{-3}) at certain points, which at very large density ratios can produce un-physical (negative) density/viscosity values and cause difficulties for computations.

We employ C^0 spectral elements for spatial discretizations of the weak forms of the equations obtained in Section 2.1 and in Appendix A. The final algorithm therefore consists of the following procedures:

(1) Solve Eq. (31) for ψ^{n+1}.
(2) Solve Eq. (32) for ϕ^{n+1}.
(3) Compute ρ^{n+1} and μ^{n+1} from Eq. (6), or from Eq. (34) for large density ratios.
(4) Compute $\nabla^2\phi^{n+1}$ from Eq. (23b), i.e. $\nabla^2\phi^{n+1}=\psi^{n+1}-\alpha\phi^{n+1}$.
(5) Solve Eq. (51) for P^{n+1}.
(6) Solve Eq. (53) for $\mathbf{u}^{n+1}$.

This algorithm has the following characteristics. First, it can deal with contact line problems with dynamic and static contact-angle boundary conditions. Second, the computations for all flow variables (velocity, pressure, phase field functions ϕ and ψ) are completely de-coupled. Third, for all flow variables only constant and time-independent coefficient matrices are involved in the linear algebraic systems after discretization, although variable density and variable viscosity are involved in the coupled Navier–Stokes/Cahn–Hilliard system. Therefore, all the coefficient matrices can be pre-computed during pre-processing. The previous two features are largely inherited from the scheme for variable-density Navier–Stokes equations [12], and they make the current algorithm very efficient. Fourth, the algorithm is formulated in weak forms, which can be readily implemented with C^0 spectral elements (or finite elements). In particular, the 4th order Cahn–Hilliard equation, together with the dynamic contact-angle boundary conditions, has been formulated into two de-coupled Helmholtz type equations. Finally, this algorithm is capable of dealing with large density ratios. We will demonstrate these points with numerical simulations in the subsequent section.

Let us briefly comment on the choice of ρ_0 and ν_m in the algorithm (Eqs. (49a) and (50a)). In [12] (see also Appendix A), these constants are chosen based on

$$\begin{cases}\rho_0=\min(\rho_1,\rho_2),\\ \nu_m\geqslant\frac{1}{2}\frac{\max(\mu_1,\mu_2)}{\min(\rho_1,\rho_2)}.\end{cases}\tag{35}$$

The above choice for the constant ν_m is very conservative. With systematic tests, we observe that the conditions for ν_m can be relaxed and that the range for the constant ρ_0 can also be expanded, as follows,

$$\begin{cases}0<\rho_0\leqslant\min(\rho_1,\rho_2),\\ \nu_m\geqslant\frac{1}{2}\left(\frac{\mu_1}{\rho_1}+\frac{\mu_2}{\rho_2}\right).\end{cases}\tag{36}$$

For the numerical simulations in Section 3 we have used $\rho_0=\min(\rho_1,\rho_2)$ and $\nu_m=\frac{1}{2}\left(\frac{\mu_1}{\rho_1}+\frac{\mu_2}{\rho_2}\right)$.

3. Numerical tests

In this section, we use two-dimensional numerical simulations to demonstrate the capabilities of the presented algorithm for contact line problems under dynamic/static contact-angle boundary conditions and involving large density ratios. We first show the spatial and temporal convergence rates of the presented algorithm using a contrived analytic solution, together with the dynamic contact-angle boundary conditions. Then we will consider several wall-bounded air–water flows, with physical parameters taking their true values, to look into the effects of static and dynamic contact angles. We will compare the simulation results with theoretical predictions and also with available experimental data.

3.1. Convergence rates

In this section we will demonstrate the spatial and temporal convergence rates of the algorithm developed in Section 2 using a contrived analytic solution.

Let us first consider the normalization of the flow variables. Let L denote a characteristic length scale, and U_0 denote a characteristic velocity scale. We normalize all length variables by L, the time by $\frac{L}{U_0}$, all velocity variables by U_0, pressure by $\rho_1U_0^2$, ψ in (23a) and (23b) by $\frac{1}{L^2}$, the variable density ρ by ρ_1, and the variable dynamic viscosity μ by μ_1.

A dimensional analysis of the system, consisting of equations (48), (5b) and (5c), with boundary conditions (7a), (7b) and (47), leads to the following non-dimensional parameters:

$$\begin{cases}\rho^*=\frac{\rho_2}{\rho_1}\ \text{(density ratio)}, & Pe=\frac{U_0\eta L}{\sigma\gamma_1}\ \text{(Peclet number)},\\ \mu^*=\frac{\mu_2}{\mu_1}\ \text{(viscosity ratio)}, & \theta_s\ \text{(static contact angle)},\\ C_n=\frac{\eta}{L}\ \text{(Cahn number)}, & D_w^*=D_wU_0\ \text{(dynamic wall mobility)},\\ Re=\frac{\rho_1U_0L}{\mu_1}\ \text{(Reynolds number)}, & We=\frac{\rho_1U_0^2L}{\sigma}\ \text{(Weber number)}.\end{cases}\tag{37}$$

Note that the mixing energy density is given by $\lambda=\frac{3}{2\sqrt{2}}\sigma\eta$, and after normalization it is $\lambda^*=\frac{\lambda}{\rho_1U_0^2L^2}=\frac{3}{2\sqrt{2}}\frac{C_n}{We}$. We normalize the numerical parameters ν_m and ρ_0 respectively as follows, $\nu_m^*=\frac{\nu_m}{\mu_1/\rho_1}\frac{1}{Re}$ and $\rho_0^*=\frac{\rho_0}{\rho_1}$. All variables below are given in non-dimensional forms.

We consider a rectangular domain $\Omega=\{(x,y):-1\leqslant x\leqslant 1,\ -1\leqslant y\leqslant 1\}$, and the following contrived time-dependent analytic solution to the coupled system of Navier–Stokes and Cahn–Hilliard equations,

$$\begin{cases}u=A\cos\pi y\sin a_0x\sin b_0t,\\ v=-\frac{Aa_0}{\pi}\sin\pi y\cos a_0x\sin b_0t,\\ P=A\sin\pi y\sin a_0x\cos b_0t,\\ \phi=A_\phi\cos ax\cos by\sin w_0t,\end{cases}\tag{38}$$

where A,a_0,b_0,A_ϕ,a,b,w_0 are prescribed constants, (u,v) are the (x,y) components of the velocity $\mathbf{u}$, and P is the effective pressure. The body force field $\mathbf{f}(\mathbf{x},t)$ in the Navier–Stokes equation (48), and the source field term $g(\mathbf{x},t)$ in the Cahn–Hilliard Eq. (5c), are chosen such that the analytic functions in (38) satisfy the coupled Navier–Stokes and Cahn–Hilliard equations (48), (5b) and (5c).

The source terms $g_c(\mathbf{x},t)$ and $g_b(\mathbf{x},t)$ in (7a) and (7b) are chosen such that the analytic solutions in (38) satisfy the dynamic contact-angle boundary conditions (7a) and (7b) on $\partial\Omega$. Dirichlet boundary conditions for the velocity, computed based on the analytic solution, are imposed on the domain boundary $\partial\Omega$. The initial conditions for the velocity and the phase field function are imposed by setting $t=0$ to the analytic solutions in (38).

To simulate this problem, we partition Ω along the x-direction into two quadrilateral spectral elements of equal sizes. We numerically integrate the coupled Navier–Stokes and Cahn–Hilliard equations in time from $t=0$ to $t=t_f$ (t_f fixed), and then compute the errors of the numerical solution against the analytic solution (38) at $t=t_f$.

The subsequent tests are performed using the following parameter values:

$$\begin{cases} A = 1.0, \quad a_0 = \pi, \quad b_0 = 1.0, \quad A_\phi = 1.0, \quad a = b = \pi, \quad w_0 = 1.0, \\ \frac{\rho_2}{\rho_1} = 3.0, \quad \frac{\mu_2}{\mu_1} = 2.0, \quad Re = 100, \quad C_n = 0.1, \quad We = 1.0607 \times 10^2, \quad Pe = 1.0607 \times 10^4, \\ \text{(static contact angle) } \theta_s = 60^0, \quad \text{(dynamic wall mobility) } D_w^* = 0.2, \\ v_m^* = \frac{v_m}{\mu_1/\rho_1}\frac{1}{Re} = \frac{1}{2}\left(\frac{\mu_1}{\rho_1} + \frac{\mu_2}{\rho_2}\right)\frac{1}{\mu_1/\rho_1}\frac{1}{Re} = 8.333 \times 10^{-3}, \\ \rho_0^* = \frac{\rho_0}{\rho_1} = \frac{1}{\rho_1}\min(\rho_1, \rho_2) = 1.0, \quad \text{(integration order) } J = 2. \end{cases} \tag{39}$$

To test the spatial convergence rate of the scheme, we use a fixed time step size $\Delta t = 0.001$, and systematically vary the order of the elements from 2 to 18. The final integration time is set to be $t_f = 0.1$ (100 time steps) in these tests. Fig. 1(a) shows the L^2 errors of the velocity, pressure, and the phase field function as a function of the element order. Note the logarithmic scale of the vertical axis. The data points exhibit an exponential decrease in the errors as the element order increases (when below element order 12). As the element order reaches 12 or above, the error curves level off around 10^{-6}. This is because at these element orders the spatial error becomes so small that the total error is saturated with the temporal error. These test results demonstrate the spatial exponential convergence rate of our scheme for the coupled Navier–Stokes/Cahn–Hilliard equations, together with the dynamic contact-angle boundary conditions.

To test the temporal convergence rate, we use a fixed large element order 18, and systematically decrease the time step size Δt from 0.1 to 0.003125. The final integration time is set to be $t_f = 1.0$ in this set of tests. In Fig. 1(b) we show the L^2 errors of the flow variables as a function of Δt, in logarithmic scales for both axes. The error curves evidently show that our algorithm achieves a second-order convergence rate in time for the coupled Navier–Stokes/Cahn–Hilliard equations together with dynamic contact-angle boundary conditions.

3.2. Equilibrium shape of a water drop on solid wall

In this subsection, we consider the equilibrium shape of a water drop (surrounded by air) on a horizontal solid wall with and without the gravity effect. The goal is to study the effects of the static contact angle and the gravity on the shape of the water drop, and to compare the simulation results with theoretical predictions for validation of static contact-angle boundary conditions. The dynamic wall mobility will therefore be set to zero in this subsection ($D_w = 0$). This test problem has been used previously by other researchers, see e.g. [13].

The water drop is initially assumed to be a semi-circle of radius R_0 with contact angle 90°, resting on the wall. Upon release, the water drop deforms to respect the contact angle set by the boundary condition. The presence of gravity also flattens the water drop. The equilibrium shape of the water drop is determined by two parameters, the static contact angle and the Eotvos number $Eo = \rho_w g_r R_0^2/\sigma$, where ρ_w is the water density, g_r is the gravitational acceleration and σ is the air–water surface tension.

A clarification about the term "contact angle" is in order at this point. The contact angle parameter θ_s in Eq. (2) and in the algorithm of Section 2 refers to the angle between the fluid–fluid interface and the solid wall measured on the side of the first fluid. In the following simulations we set air as the first fluid and water as the second fluid. Therefore, θ_s in the algorithm corresponds to the contact angle measured *on the air side*. In contrast, in the literature the term "contact angle" for the air/water system by default refers to the angle between the air–water interface and the wall measured *on the water side*. We will qualify the term "contact angle" with "air-side" or "water-side" where confusion may arise.

The physical parameters (air/water density, viscosity, surface tension) involved in the problem all assume their true physical values. Specifically,

$$\begin{cases} \text{air}: & \rho_1 = 1.2041 \text{ kg/m}^3 \\ & \mu_1 = 1.78 \times 10^{-5} \text{ kg/(m s)} \\ \text{water}: & \rho_2 = \rho_w = 998.207 \text{ kg/m}^3 \\ & \mu_2 = 1.002 \times 10^{-3} \text{ kg/(m s)} \\ \text{surface tension}: & \sigma = 7.28 \times 10^{-2} \text{ kg/s}^2 \\ \text{gravity}: & g_r = 9.8 \text{ m/s}^2. \end{cases} \tag{40}$$

We normalize the flow variables in the same way as in Section 3.1. We choose the characteristic length scale $L = R_0 = 1$ cm, the characteristic velocity scale $U_0 = \sqrt{g_0 L}$, where $g_0 = 1 \text{ m/s}^2$ for this problem. In addition to the non-dimensional parameters in (37), this problem also involves the Froude number, $Fr = \frac{U_0}{\sqrt{g_r L}}$, or equivalently, the Eotvos number Eo as defined previously. We use the Eotvos number in the following discussions. The physical parameter values result in a density ratio $\frac{\rho_2}{\rho_1} = 829$, a dynamic viscosity ratio $\frac{\mu_2}{\mu_1} = 56.29$, a Reynolds number $Re = \frac{\rho_1 U_0 L}{\mu_1} = 67.65$, and a Weber number $We = 1.654 \times 10^{-3}$. In the simulations we use a

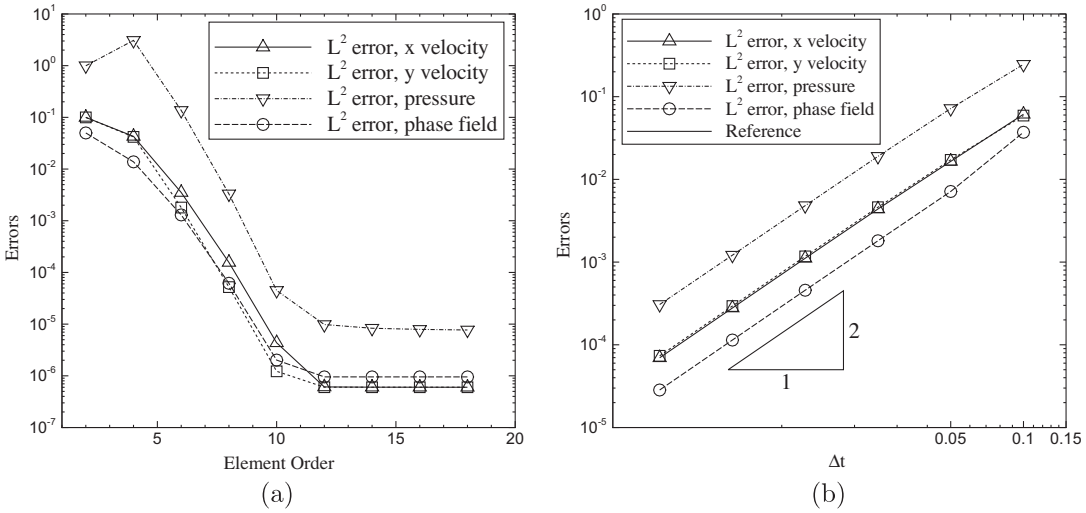

Fig. 1. Convergence rates: L^2 errors of velocity, pressure and phase field function as a function of element order (a), and as a function of time step size Δt (b), showing spatial exponential convergence rate and temporal second-order convergence rate. In (a) a fixed $\Delta t = 0.001$ is used, and in (b) a fixed element order 18 is used.

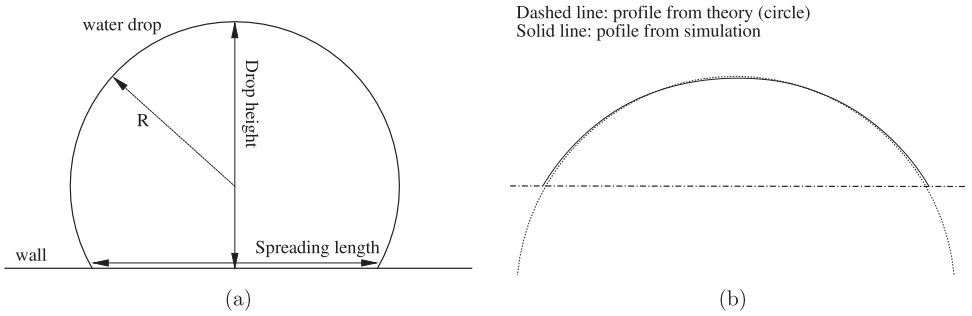

Fig. 2. Equilibrium shape of a water drop on the wall (no gravity): (a) Sketch showing parameters; (b) comparison of equilibrium shapes between simulation and theory for water-side static contact angle 60°.

Cahn number $C_n = 0.01$ and a Peclet number $Pe = 1.061 \times 10^2$. No dynamic wall mobility effect is considered in this problem, and so $D_w^* = 0$.

3.2.1. No gravity ($Eo = 0$)

In the absence of gravity ($Eo = 0$) the surface tension is the only force that comes into play. The equilibrium shape of the water drop is a circular cap that respects the contact angle at the wall [6]; see Fig. 2(a) for a sketch of the shape and the definition of related parameters. Let R denote the radius of circle at equilibrium, θ_E denote the water-side static contact angle, L_s denote the spreading length on the wall, and H denote the drop height. By conservation of volume of the water drop, we have

$$\frac{R}{R_0} = \sqrt{\frac{\pi/2}{\theta_E - \sin\theta_E \cos\theta_E}}, \quad L_s = 2R\sin\theta_E, \quad H = R(1-\cos\theta_E). \tag{41}$$

Consider a flow domain (non-dimensional), 6.0×2.0 ($-3 \leqslant x \leqslant 3$, $0 \leqslant y \leqslant 2$). We assume that the top and bottom boundaries of the domain ($y = 0$ and 2) are solid walls, and that the boundaries in the x direction are periodic. The water drop initially has a radius R_0 (semi-circle), and is located in the middle of the bottom wall.

The flow domain is discretized with 768 equal-sized quadrilateral elements, with 48 and 16 elements, respectively in x and y directions. We use an element order 14 for all elements in the simulations. The time step size is set to $\Delta t = 5 \times 10^{-5}$.

Fig. 2(b) shows the equilibrium profile of the water drop from the simulation for a water-side static contact angle 60^0. For comparison, we have also shown the theoretical shape [6] of the water drop for this case (see Eq. (41)). The profiles of the water drop from the simulation and from the theory are qualitatively very close.

For a quantitative comparison, Fig. 3 shows the numerical values of the spreading length and drop height, normalized by R_0, as a function of the static contact angle θ_E between simulation and the theoretical results from Eq. (41). The contact angle ranges from 15° to 165° in our simulations. For the contact angle 15°, we have used a different flow domain (8.75×1.25) to accommodate the large spreading length, and have taken the equilibrium shape corresponding to the contact angle 30° as the initial water drop profile. We observe that overall the simulation results agree with the theoretical values quite well for both the spreading length and the drop height. However, we observe a larger discrepancy between simulation and theory in the spreading length for very small and very large contact angles ($\theta_E = 15°$ and 165°).

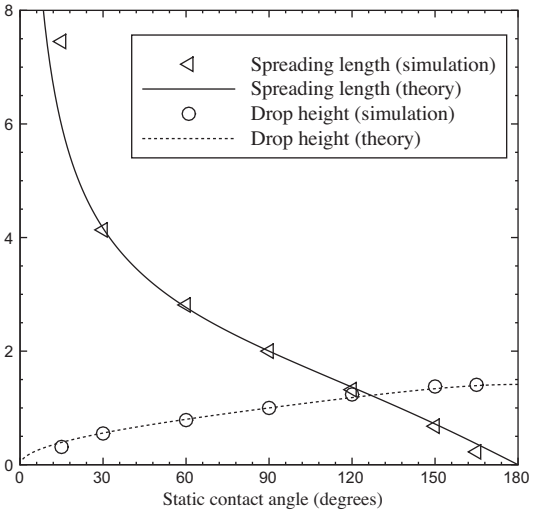

Fig. 3. Comparison of spreading length and drop height (normalized by R_0) as a function of static contact angle between simulation and theory (no gravity).

3.2.2. Effect of gravity ($Eo \neq 0$)

When the gravity is present, the shape of the water drop is determined by the balance of three effects: (i) the gravity which tends to spread the drop onto the wall, (ii) the surface tension which tends to restore the drop to a circular cap, and (iii) the contact angle condition which the drop shape must satisfy at the wall. If $Eo \ll 1$, the surface tension dominates and the drop assumes the shape of a circular cap with contact angle θ_E, where the drop height H_0 is given by

$$\frac{H_0}{R_0} = (1-\cos\theta_E)\sqrt{\frac{\pi/2}{\theta_E - \sin\theta_E\cos\theta_E}}. \tag{42}$$

If $Eo \gg 1$, the gravity dominates and the water forms a puddle. The drop height (thickness of puddle) H_∞ is given by [6]

$$\frac{H_\infty}{R_0} = \frac{2}{R_0}\sqrt{\frac{\sigma}{\rho_w g_r}}\sin\left(\frac{\theta_E}{2}\right) = \frac{2}{\sqrt{Eo}}\sin\left(\frac{\theta_E}{2}\right). \tag{43}$$

We employ the same values for the physical and mesh parameters as in the previous case with no gravity. We systematically vary the Eotvos number by varying the gravitational acceleration g_r. The time step size is the same as that of the case with no gravity for small Eo values. For larger Eotvos numbers ($Eo > 5$), we use a smaller time step size $\Delta t = 2.5 \times 10^{-5}$.

Fig. 4 shows profiles of the air–water interface for $Eo = 0.137$ (a), $Eo = 1.37$ (b), and $Eo = 13.7$ (c) from the simulations, for a static contact angle 120°. It is evident that the water drop resembles a circular cap at small Eo and a puddle at large Eo. The water drop has a shape that resembles an elongated circular cap at $Eo \sim 1$,

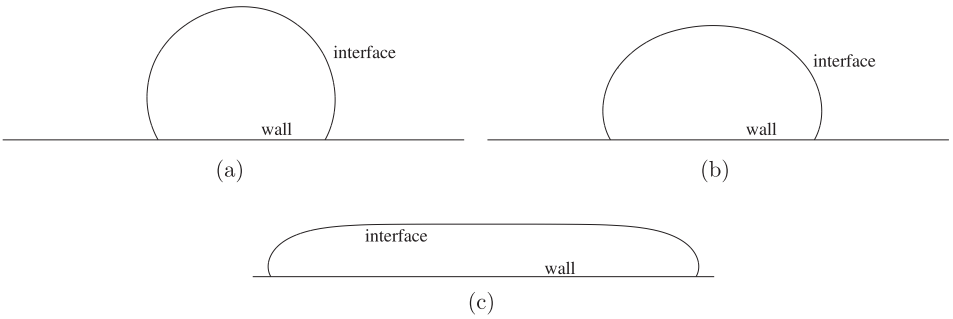

Fig. 4. Profiles of air–water interface with Eotvos numbers (a) $Eo = 0.137$, (b) $Eo = 1.37$, and (c) $Eo = 13.7$. Static contact angle is 120°.

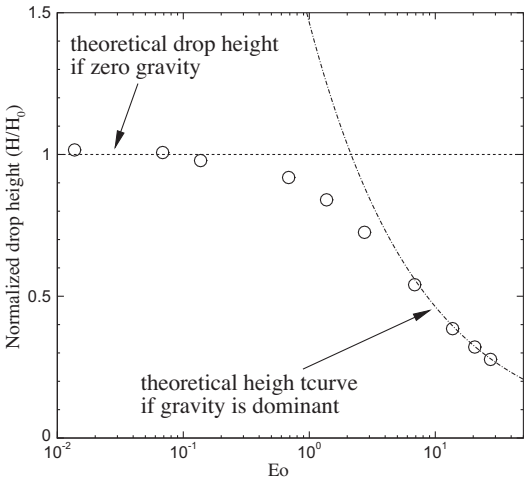

Fig. 5. Normalized drop height as a function of Eotvos number (static contact angle 120^0). Symbols denote data from simulations.

where the relative importance of the surface tension and the gravity is comparable.

In Fig. 5 we plot the height of the water drop, normalized by the theoretical drop height under zero gravity H_0 (Eq. (42)), as a function of the Eotvos number, for a fixed static contact angle 120^0 from the simulations. For comparison we have also marked the theoretical drop height under zero gravity, and shown the curve for the theoretical drop height for large Eotvos numbers (Eq. (43)). The simulation results are in good agreement with the asymptotic solutions given by (42) and (43) at small and large *Eo* values, and one can also observe a transition in between for moderate *Eo* values.

3.3. Bouncing water drop on a hydrophobic wall

In this subsection we consider the bouncing of a small water drop on a hydrophobic wall. The bouncing water drop on hydrophobic surfaces has been the subject of a number of existing experimental studies; see e.g. [29,37] and the references therein. The goal of this test is to demonstrate the capability of the presented algorithm for dealing with static and dynamic contact angles at realistic air–water density ratios and viscosity ratios. We will also compare simulation results with the available experimental data.

We choose a characteristic length scale $L = 5$ mm, and a characteristic velocity scale $U_0 = \sqrt{g_0 L}$, where $g_0 = 1\ \mathrm{m/s^2}$. Consider a non-dimensional flow domain, $\Omega = \{(x,y) : -1/2 \leqslant x \leqslant 1/2,\ 0 \leqslant y \leqslant 3/2\}$. A circular water drop, surrounded by air, is contained in Ω and is initially at rest. The water drop has a non-dimensional radius $R_0 = 1/4$, and its center is located initially at $(x_0, y_0) = (0, 1.0)$. The gravity is assumed to be in $-y$ direction. We assume that the top and bottom boundaries (i.e. $y = 0$ and $3/2$) of the domain are solid walls, with no-slip conditions for the velocity and dynamic contact-angle conditions for the phase field function. On the boundaries in the horizontal direction ($x = \pm 1/2$), we assume periodic conditions for all flow variables (velocity, pressure, phase field function), with one exception. If the water-side static contact angle is 90° or less (i.e. $\theta_E \leqslant 90^\circ$), we will assume that the domain boundaries at $x = \pm 1/2$ are also solid walls. This exception in setting is in consideration of the fact that, at these contact angles in the current setting, the water drop will break up at the bottom wall and form a pool at the bottom of the domain.

The water drop falls through the air under gravity, and impacts the bottom wall. When the water-side contact angle is sufficiently large (hydrophobic), the drop will bounce off the bottom wall and the bouncing may repeat several times. We will simulate this process in the current problem.

The normalization of flow variables follows the discussions in Section 3.2. The physical parameter values are provided in (40). As a result, we have a density ratio $\frac{\rho_2}{\rho_1} = 829$, a dynamic viscosity ratio $\frac{\mu_2}{\mu_1} = 56.29$, a Reynolds number $Re = \frac{\rho_1 U_0 L}{\mu_1} = 23.92$, a Weber number $We = 4.135 \times 10^{-4}$, and a Froude number $Fr = 0.319$. We employ a Cahn number $C_n = 0.01$ and a Peclet number $Pe = 1.061 \times 10^2$ in the simulations.

We discretize the domain Ω using a mesh of 150 quadrilateral elements of equal sizes, with 10 elements in the x-direction and 15 elements along the y-direction. An element order 14 has been employed for all elements. The static contact angle parameter θ_s and the non-dimensional dynamic wall mobility D_w^* are varied in the tests to modify the wall hydrophobicity in order to demonstrate the effects of the static and dynamic contact angles.

The initial phase field function is set to the following hyperbolic tangent function

$$\phi_0(\mathbf{x}) = \tanh \frac{\|\mathbf{x} - \mathbf{X}_0\| - R_0}{\sqrt{2} C_n}, \tag{44}$$

where $\mathbf{X}_0 = (x_0, y_0)$ is the initial coordinate of the center of mass of the water drop, and C_n is the Cahn number. Zero initial condition is used for the velocity field.

Let us first consider only the effect of the static contact angle on the behavior of the water drop, by setting $D_w^* = 0$. We have performed simulations with several water-side static contact angles: 165°, 150°, 120°, 90° and 60°. The first three values correspond to hydrophobic walls, and the last case corresponds to a hydrophilic wall. With contact angles 90° and 60°, the water drop does not bounce on the wall. Instead, it changes topology on impact to the bottom wall, and forms a water pool to fill up the bottom of the container. Note that in these two cases, solid walls have been assumed on all domain boundaries. Repeated bouncing has been

observed at contact angles 165° and 150°, while the water drop barely bounces at a contact angle 120°.

We will demonstrate the general behavior of the water drop using a temporal sequence of snapshots of its configurations. Fig. 6 shows such a sequence for contact angle 165°. Plotted are the contour level $\phi(\mathbf{x}, t) = 0$ at a number of time instants. Note that this temporal sequence covers only the first bounce of the water drop. Figs. 6(a)–(c) show the free fall of the water drop through the air. Upon impact of the bottom wall (Figs. 6(d)–(f)), the water drop spreads horizontally on the wall and deforms drastically, forming a pancake-like shape (Fig. 6(f)). Then it retracts in the horizontal direction and starts to restore its circular shape, as shown in Figs. 6(g)–(i). Note that the drop appears to have trapped a thin pocket of air between itself and the bottom wall; see Figs. 6(e)–(h). The snapshots in Figs. 6(j)–(n) show that the water drop bounces off the bottom wall after impact and rises through the air, reaching

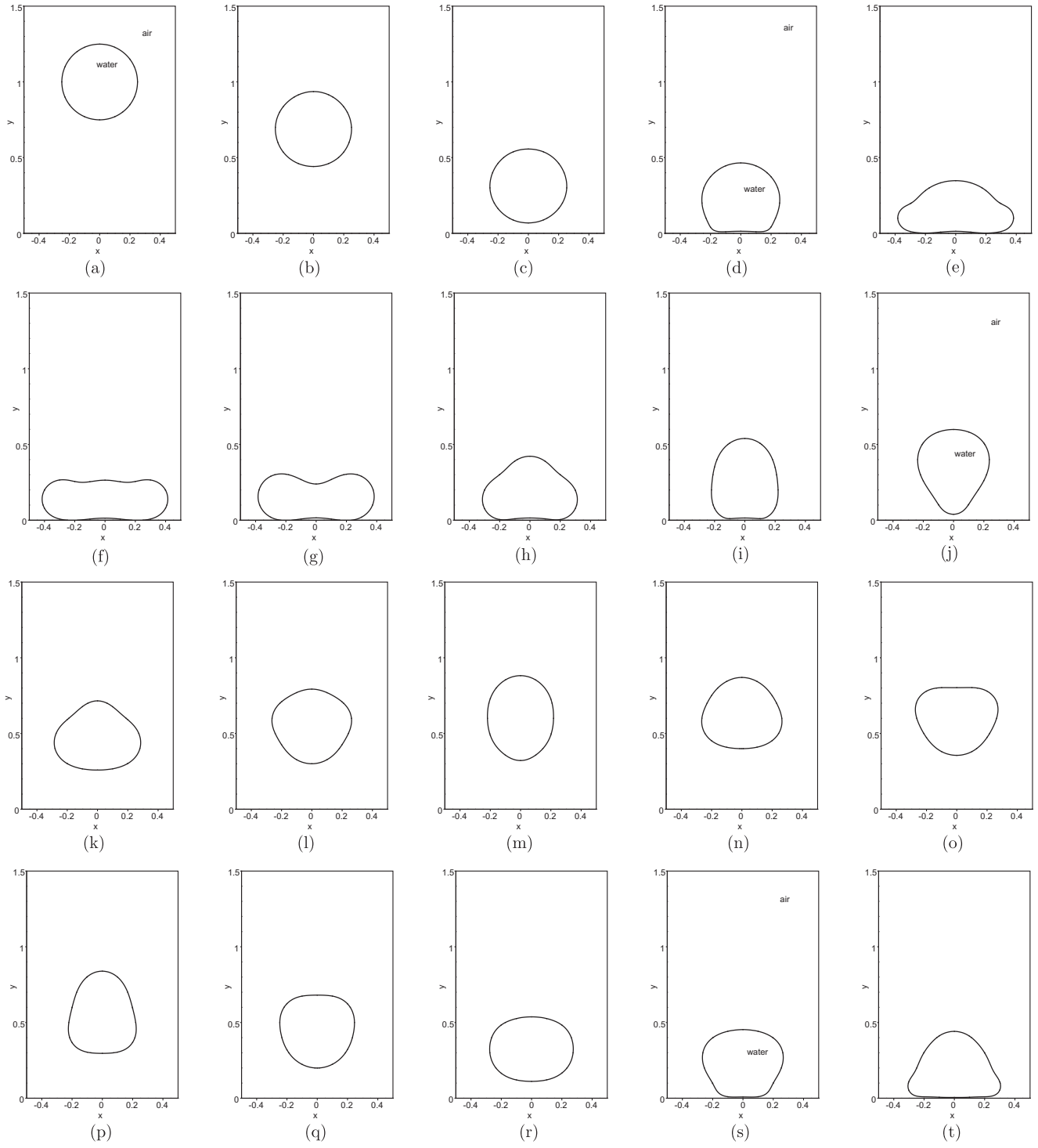

Fig. 6. Snapshots of a bouncing water drop on a hydrophobic wall with water-side static contact angle 165° ($D_w^* = 0$): (a) $t = 0.0125$, (b) $t = 0.2625$, (c) $t = 0.3875$, (d) $t = 0.4125$, (e) $t = 0.45$, (f) $t = 0.4875$, (g) $t = 0.525$, (h) $t = 0.5625$, (i) $t = 0.6$, (j) $t = 0.6375$, (k) $t = 0.7$, (l) $t = 0.7625$, (m) $t = 0.825$, (n) $t = 0.8875$, (o) $t = 0.95$, (p) $t = 1.0125$, (q) $t = 1.075$, (r) $t = 1.1375$, (s) $t = 1.175$, (t) $t = 1.2$.

a maximum height about 0.6 (Fig. 6(n)). Then the water drop falls through the air and impacts the bottom wall again (Figs. 6(o)–(t)). We can observe significant drop deformation and its shape oscillation during the rising and falling process.

The behavior of the water drop differs notably as the contact angle is changed. As the water-side contact angle decreases (less hydrophobic), we observe that the water drop becomes less likely to bounce off the wall upon impact, and that the number of bounces tends to decrease even if it does. In Fig. 7 we demonstrate the behavior of the water drop for a contact angle 120° using a temporal sequence of snapshots, which can be compared with that in Fig. 6 for contact angle 165°. We observe that with the smaller contact angle °120° the drop barely bounces off the wall after the impact; see Fig. 7(l). The small air bubble, initially trapped between the water drop and the bottom wall (Figures 7(e)–(k)), escapes from below the water drop after it slightly lifts off from the wall (Figs. 7(k)–(l)). After that, the water drop attaches to the bottom wall, and no longer lifts off again. The drop shape oscillates

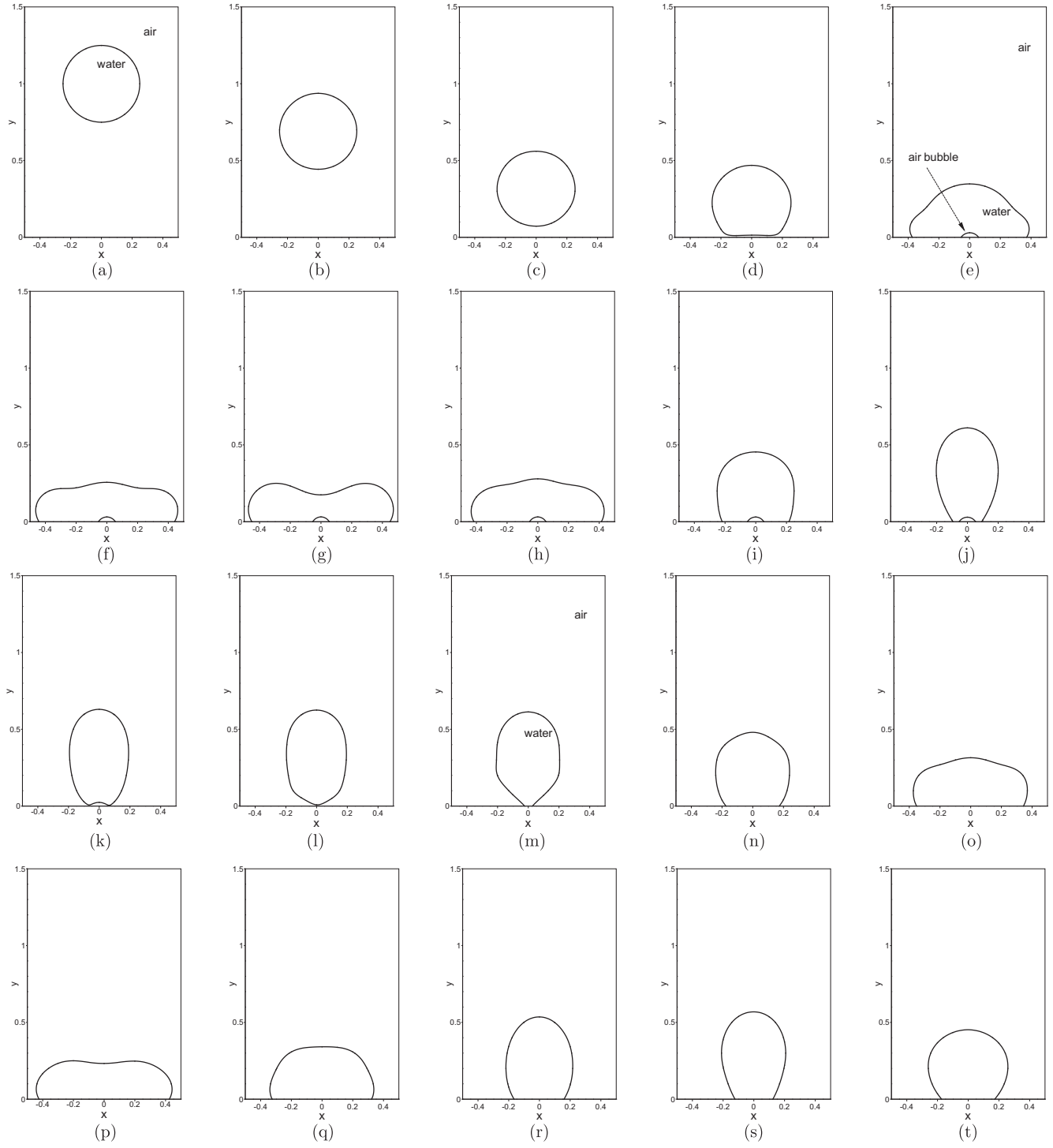

Fig. 7. Snapshots of a bouncing water drop on a hydrophobic wall with a water-side static contact angle 120° ($D_w^* = 0$): (a) $t = 0.0125$, (b) $t = 0.2625$, (c) $t = 0.3875$, (d) $t = 0.4125$, (e) $t = 0.45$, (f) $t = 0.4875$, (g) $t = 0.525$, (h) $t = 0.575$, (i) $t = 0.6375$, (j) $t = 0.7$, (k) $t = 0.725$, (l) $t = 0.7375$, (m) $t = 0.75$, (n) $t = 0.825$, (o) $t = 0.8875$, (p) $t = 0.95$, (q) $t = 1.0125$, (r) $t = 1.075$, (s) $t = 1.1375$, (t) $t = 1.2$.

quasi-periodically, spreading/compressing alternately along the horizontal and vertical directions; see Figs. 7(m)–(t).

Let us now consider the motion of the center of mass of the water drop, defined by

$$\mathbf{X}_c = (x_c, y_c) = \frac{\int_{\Omega_w} \mathbf{x} dA}{\int_{\Omega_w} dA}, \tag{45}$$

where Ω_w denotes the region occupied by the water drop. Fig. 8 shows time histories of the y coordinate of the center of mass corresponding to contact angles 165°, 150° and 120°. We note first the oscillatory nature of the time histories and the attenuation of the oscillation amplitudes over time. The first few oscillations correspond to the bounce-off of the water drop from the wall. Specifically, for contact angles 165° and 150°, the first 5 and the first 4 oscillations respectively correspond to the bounce off the wall, while for the contact angle °120° only the first one corresponds to the bounce-off. In the time histories, the oscillations beyond the first few periods correspond to the shape oscillation of the water drop, alternately spreading/compressing in vertical and horizontal directions. One can also observe a difference in the oscillation periods with respect to the contact angle. The oscillation period appears to decrease with decreasing contact angle.

From the data about the center of mass we can determine the restitution coefficient. Following [29], we define the restitution coefficient ϵ_r by

$$\epsilon_r = \sqrt{\frac{H'}{H}}, \tag{46}$$

where H and H' are respectively the maximum heights of the water drop above the wall before and after the bounce. We will also follow [29] to estimate the impact velocity V of the water drop using $V \approx \sqrt{2g_r H}$, where g_r is the gravitational acceleration.

In Fig. 9 we show the restitution coefficient as a function of the impact velocity for contact angle 165^0 from our simulations. The experimental values of restitution coefficient from [29] are also shown in the figure for comparison. The experimental data are for a comparable contact angle 170^0, and the drop sizes are smaller than that employed in the current simulation. Overall, we observe that the simulation results agree with the experimental data reasonably well. The two data points from simulation for impact velocities 0.25 m/s and 0.31 m/s, which correspond to the first two bounces in Fig. 8, have a somewhat larger difference compared to the bulk of experimental data. This difference is likely caused by

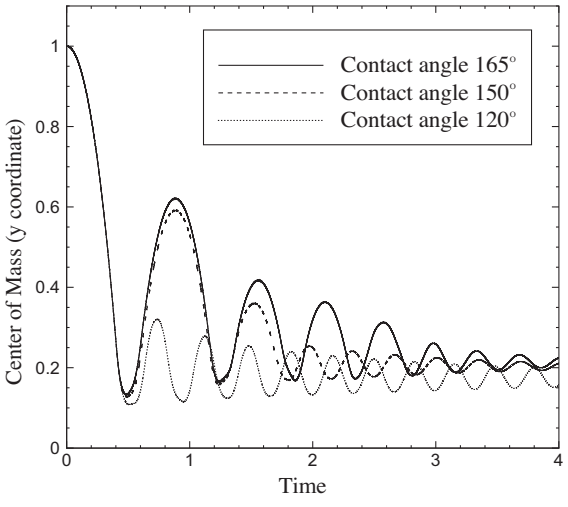

Fig. 8. Time histories of the water-drop center of mass (y coordinate) for different static contact angles.

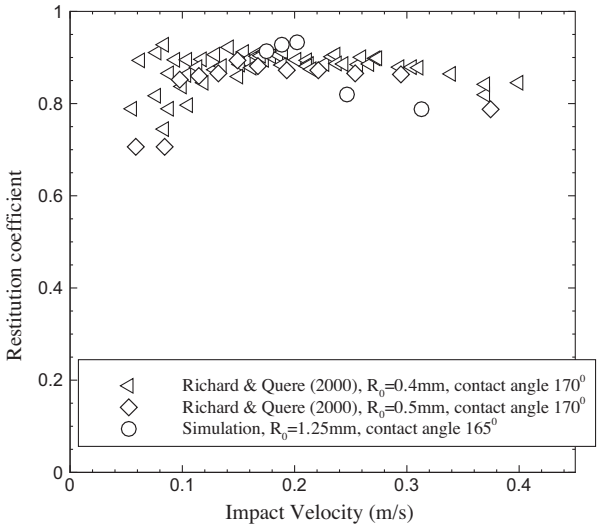

Fig. 9. Comparison of the coefficient of restitution as a function of the impact velocity between current simulation and the experiment of [29].

the larger drop size used in current simulations, which results in significant deformations of the water drop upon impact and strong oscillations in the shape after it bounces off the wall (Fig. 6). Drop deformation stores elastic energy, thus reducing the maximum height the drop can reach after the bounce and leading to a smaller restitution coefficient. This is in contrast to the small drop deformations in the experiment of [29]. On the other hand, after the first two bounces, we observe in the simulation that, the drop deformation and the oscillation in its shape become dramatically weaker. Accordingly, one can observe from Fig. 9 that, the simulation data points corresponding to these later bounces (with smaller impact velocities, about ~ 0.2 m/s or less) are very close to the experimental values.

Let us now look into the effects of the static contact angle on the profiles of the air–water interface (i.e. water drop configuration) upon impact to the wall. Fig. 10 shows the interfacial profiles (contour level $\phi = 0$) at an instant ($t = 0.4375$) during the initial impact of the water drop on the bottom wall, corresponding to water-side static contact angles ranging from 165° to 60°. For contact angle 165°, the air–water interface appears still intact, which traps a thin cushion of air between the bottom wall and the water (Fig. 10a). For the other smaller contact angles, the interface has broken up into two pieces. The inner piece of the interface traps a thin air cushion or a small air bubble between the wall and the water, while the outer piece separates the water from the bulk of air (Figs. 10(b)–(e)). At this moment, the contact lines formed between the outer interface and the bottom wall are spreading outwards in the horizontal direction. It is evident that the overall drop shape and configuration are strongly dependent on the contact angle. On a hydrophobic wall (contact angle $> 90°$), the impact results in a rim in the drop shape which is located above the wall and bulges outward (Figs. 10(a)–(c)), while on a hydrophilic wall (contact angle $< 90°$) or a wall with contact angle 90° the rim of the water drop is located on the wall (Fig. 10(d)–(e)).

In the above tests we have ignored the effect of the dynamic wall mobility. Let us now take this effect into account. We will concentrate on a water-side static contact angle 120^0, and investigate the effects of different dynamic wall mobility values.

We first look into the behavior of the water drop under dynamic contact-angle boundary conditions. Fig. 11 shows a temporal sequence of snapshots of the water drop (contour level $\phi = 0$) for a water-side static contact angle 120° and dynamic wall mobility $D_w^* = 0.2$. The plots can be compared with those of Fig. 7, in which

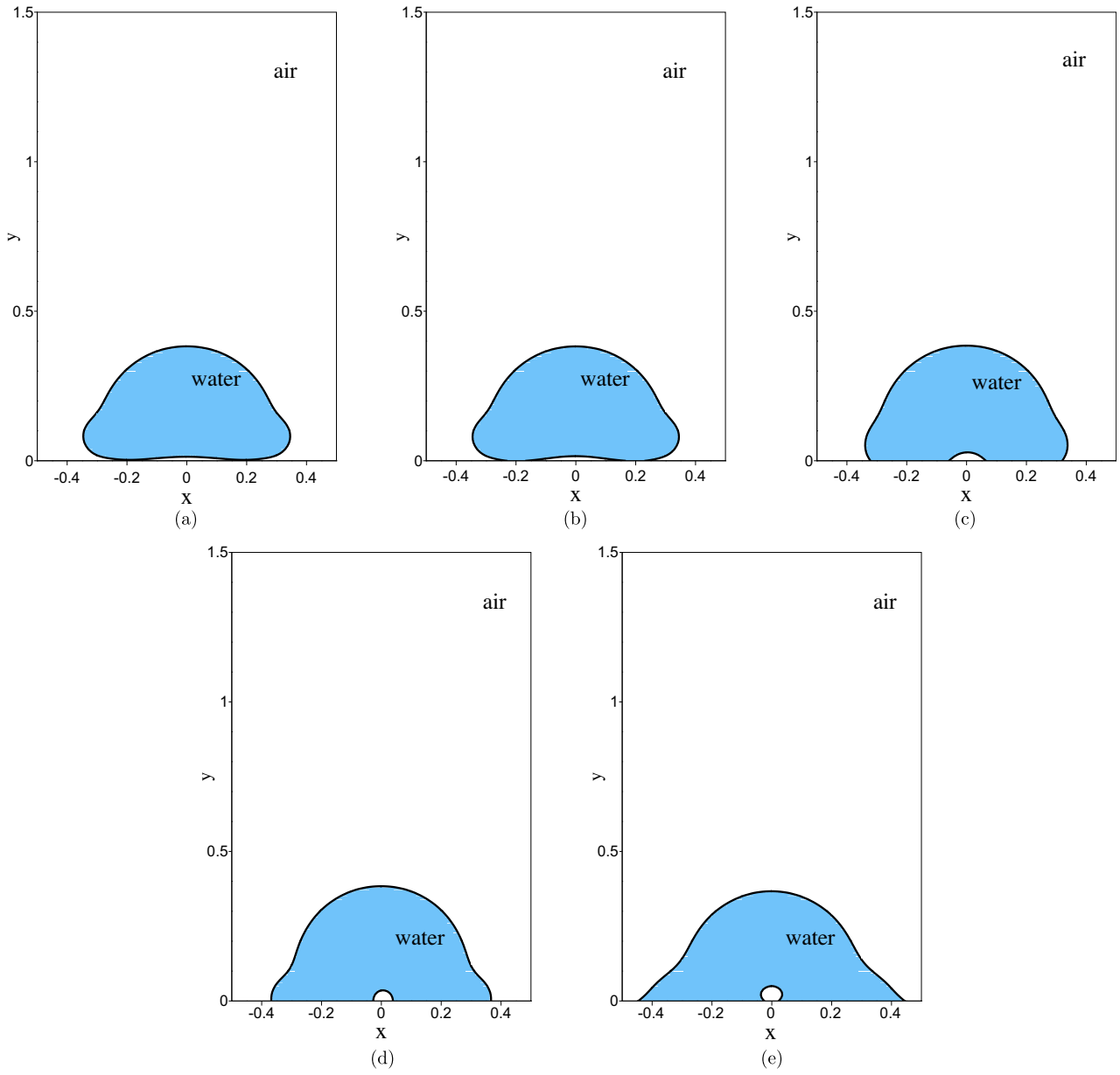

Fig. 10. Effect of static contact angles: Profiles of the air–water interface at $t = 0.4375$ (first bounce/impact on bottom wall) with water-side static contact angles 165° (a), 150° (b), 120° (c), 90° (d), and 60° (e). Water occupies the shaded (or light blue) region. (For interpretation of the references to colour in this figure legend, the reader is referred to the web version of this article.)

the dynamic wall mobility effect is ignored. First, we observe that in this case the water drop does not bounce at all. In contrast, without dynamic wall mobility, the water drop slightly bounces off the wall after the first impact. Second, the most prominent effect of the dynamic wall mobility appears to be retarding the motion of the air–water interface. One can observe that in the presence of dynamic wall mobility the oscillation in the drop shape attenuates more significantly and the water drop settles down on the wall sooner. In contrast, with zero dynamic wall mobility, the drop shape oscillates for many times and it takes a longer time for the drop to eventually settle down on the wall (see Fig. 8). Third, the dynamic wall mobility induces a notable deviation of the instantaneous contact angle from the static contact angle; see e.g. Fig. 11(e) and Fig. 11(h). As the water drop settles on the wall and the contact-line motion wanes, the instantaneous contact angle gradually relaxes to the static contact angle (Fig. 11(o)). We will elaborate on the last point in subsequent discussions.

The effect of the dynamic wall mobility on the drop motion is demonstrated by Fig. 12, in which we plot the y coordinate of the center of mass as a function of time for several D_w^* values ranging from 0.0 to 0.5. In the absence of dynamic wall mobility ($D_w^* = 0$), the time-history curve is highly oscillatory and the amplitude attenuation is very slow. It therefore takes a long time for the water drop to eventually settle down on the wall with only the static contact-angle effect. In the presence of dynamic wall mobility, the time-history curve is still oscillatory, but the oscillation amplitude attenuates more rapidly. Moreover, the attenuation becomes stronger with increasing D_w^* values, indicating that the drop settles on the wall sooner as D_w^* increases. Fig. 12 also indicates that the oscillation period decreases as D_w^* increases.

Let us now look more closely into the effect of D_w^* on the dynamic (instantaneous) contact angle. Fig. 13 shows configurations of the water drop at two time instants $t = 0.45$ and $t = 0.6125$ for a fixed static contact angle 120°, but obtained with different D_w^*

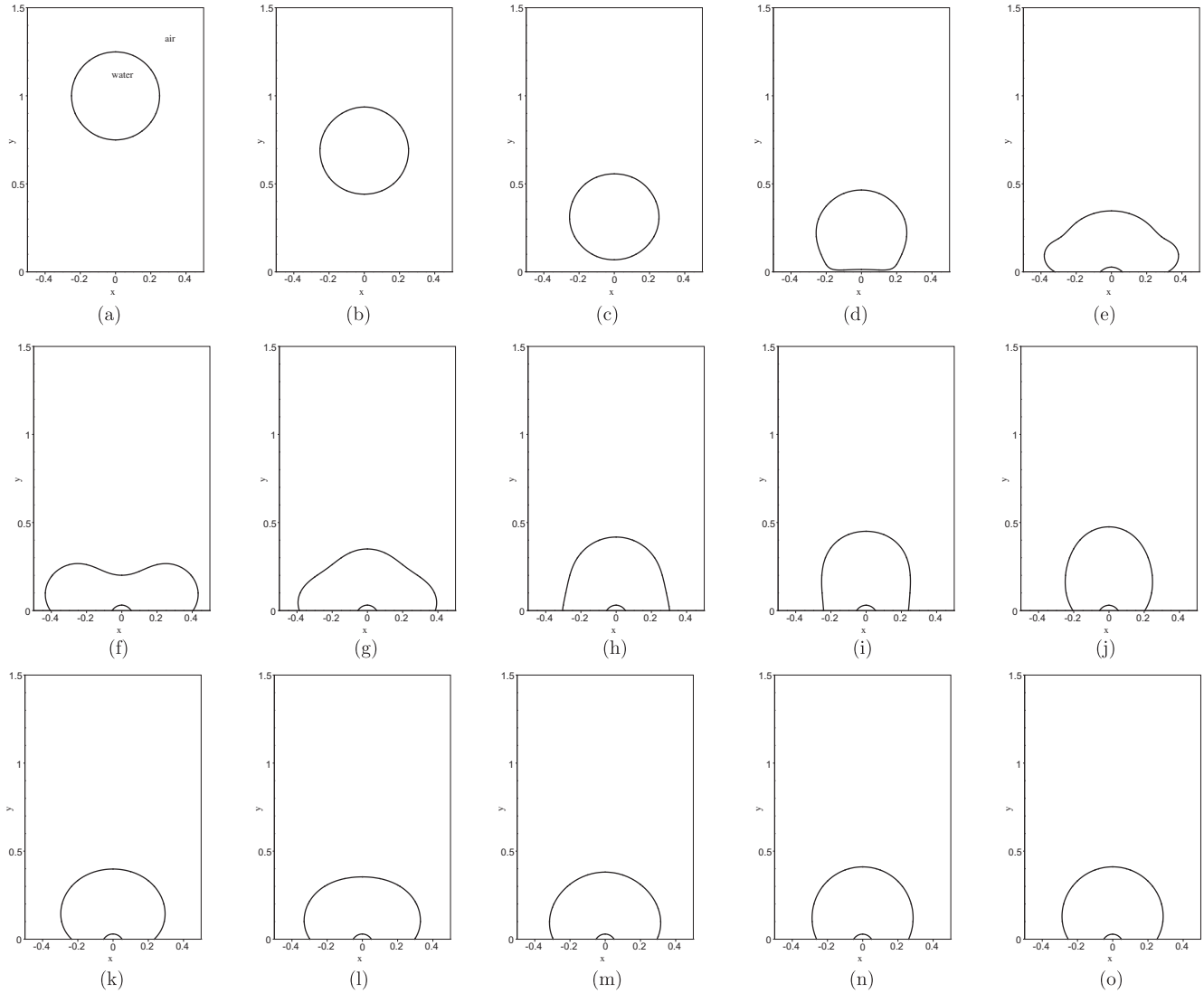

Fig. 11. Snapshots of bouncing water drop with dynamic wall mobility $D_w^* = 0.2$ (static contact angle 120°): (a) $t = 0.0125$, (b) $t = 0.2625$, (c) $t = 0.3875$, (d) $t = 0.4125$, (e) $t = 0.45$, (f) $t = 0.5125$, (g) $t = 0.575$, (h) $t = 0.6125$, (i) $t = 0.6375$, (j) $t = 0.7$, (k) $t = 0.7625$, (l) $t = 0.825$, (m) $t = 0.8875$, (n) $t = 0.95$, (o) $t = 1.0125$.

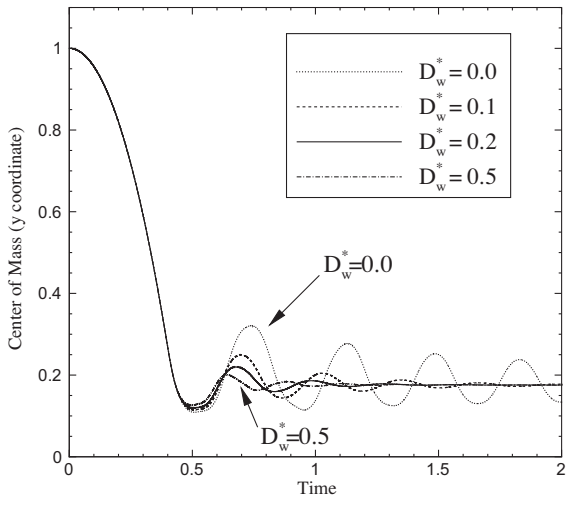

Fig. 12. Time histories of the water-drop center of mass computed with different dynamic wall mobilities (static contact angle 120°).

values. At the instant $t = 0.45$, the contact lines formed between the bottom wall and the outer air–water interface are moving outward on the bottom wall. The solid arrows in Fig. 13(a) indicates the directions of the contact-line motions. The water-side angle between the interface and the wall therefore corresponds to an advancing contact angle at this instant. At $t = 0.6125$, these contact lines are moving inward on the bottom wall; see the solid arrows in Fig. 13(e). The angle between the interface and the wall therefore corresponds to a receding contact angle at this moment. With $D_w^* = 0$, no difference is observed in the advancing and receding contact angles; see Figs. 13(a) and (e). Both correspond to the static contact angle. If $D_w^* \neq 0$, the advancing and receding contact angles are evidently different from the static contact angle. One can observe an advancing contact angle that is larger, and a receding contact angle that is smaller, than the static contact angle. Furthermore, as D_w^* increases, the deviation of the advancing/receding contact angles from the static one become more pronounced; see Figs. 13(d) and (h).

In Fig. 14 we show patterns of the instantaneous velocity fields computed with a static contact angle 120° and different dynamic wall mobility D_w^* values, at the same two time instants as those of Fig. 13. The plots (a) and (b) are computed with $D_w^* = 0.0$, and

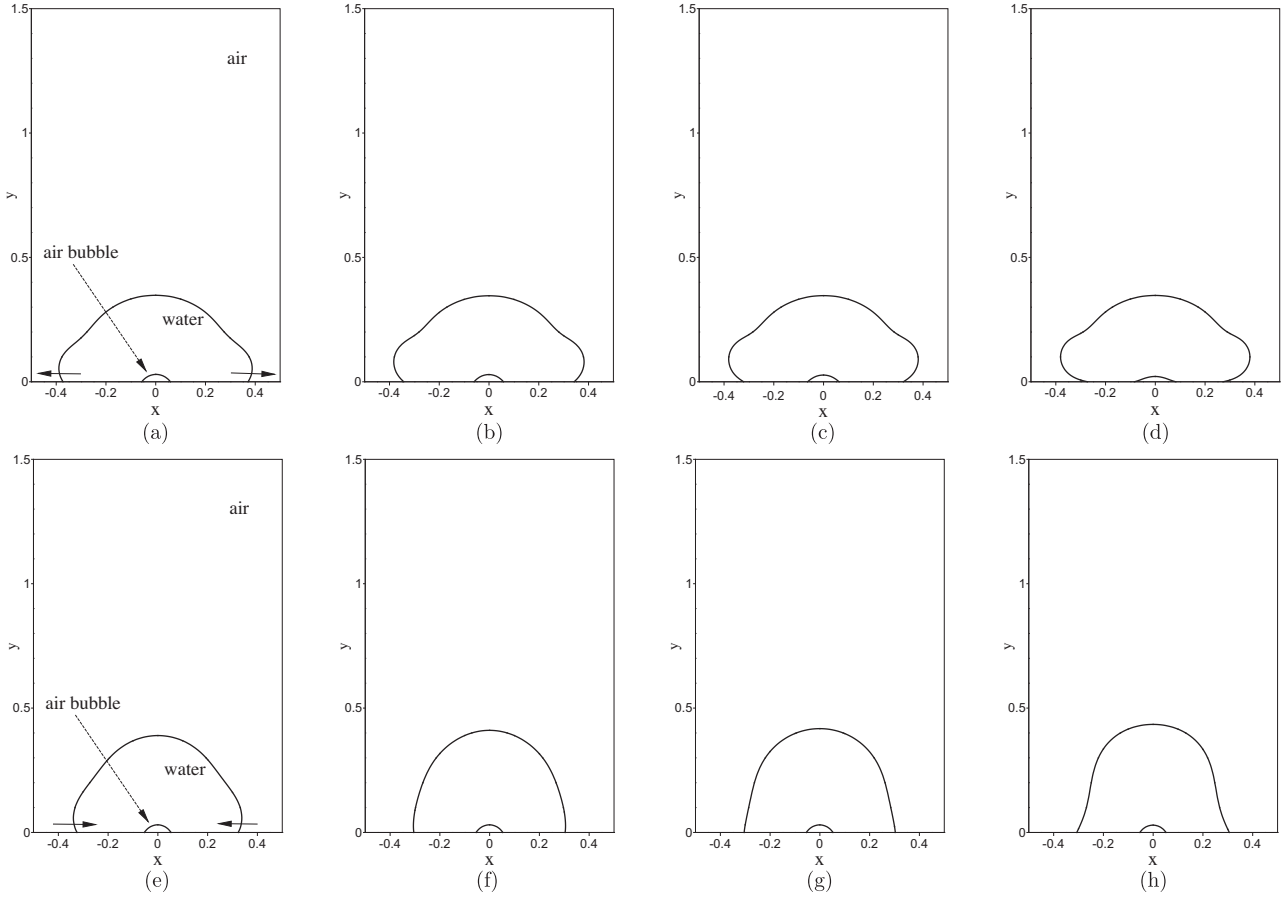

Fig. 13. Effect of dynamic wall mobility on advancing/receding contact angles (static contact angle 120°): Profiles of air–water interface at two time instants: $t = 0.45$ (top row) and $t = 0.6125$ (bottom row). (a) and (e), $D_w^* = 0.0$; (b) and (f), $D_w^* = 0.1$; (c) and (g), $D_w^* = 0.2$; (d) and (h), $D_w^* = 0.5$. In top-row plots, contact lines are moving outward, see the solid arrows in (a). In bottom-row plots, contact lines are moving inward, see the solid arrows in (e).

(c) and (d) are for $D_w^* = 0.2$. The plots (a) and (c) are at time instant $t = 0.45$, and (b) and (d) are for $t = 0.6125$. Figs. 14(a) and 14(b) correspond respectively to the air–water interfacial profiles shown in Figs. 13(a) and 13(e), and Figs. 14(c) and 14(d) correspond respectively to Figs. 13(c) and 13(g). The velocity vectors are plotted on the quadrature points of the spectral elements, which are non-uniform and clustered on the element boundaries. This gives rise to the "striped" patterns in the plots because more velocity vectors are located on the element boundaries. For clarity, we have shown only the bottom third of the container in the plots. At $t = 0.45$ (Figs. 14(a,c)), the water drop is spreading outward along the bottom wall and the drop height is decreasing. Displaced by the water, the air originally located near the bottom wall rises along the domain boundaries at $x = \pm\frac{1}{2}$, forming a pair of vortices. Note that periodic boundary conditions are used in the horizontal direction. In addition, one can observe a strong shear around the "shoulder" region of the water drop caused by the relative motions of the water and air. At $t = 0.6125$ (Figs. 14(b,d)), the horizontal dimension of the water drop is decreasing and the drop height is growing. One can observe that the flow field inside the water region follows this general trend. It is also evident from the velocity patterns that the ambient air rushes in toward the bottom wall to fill in the space vacated by the water drop as it retracts along the bottom wall. One can again observe a velocity shear in the shoulder region of the water drop. A comparison between Figs. 14(a) and (c), and between Figs. 14(b) and (d), indicates that the overall patterns of the velocity field with $D_w^* = 0.0$ and $D_w^* = 0.2$ are quite similar to each other. Some differences in the velocity distribution can be discerned between these D_w^* values in the near-wall regions around the moving contact lines, especially at $t = 0.6125$.

To summarize, the bouncing water drop problem involves a large density ratio ($\rho_2/\rho_1 \approx 829$), and the drop behavior (bounce or the lack thereof) depends strongly on the hydrophobicity of the wall. The results show that our algorithm can effectively deal with the static and dynamic contact-angle boundary conditions for two-phase problems involving large density ratios. The method has produced results that are in good agreement with the experimental data. We have shown that the static contact angle and the dynamic wall mobility strongly influence the behavior of the water drop. A prominent effect of the dynamic wall mobility is to retard the motion of the air–water interface, inducing a strong attenuation in the drop-shape oscillation and large deviations of the instantaneous contact angle from the static contact angle.

3.4. Water drop moving down a slope

In this subsection we consider a water drop moving down an inclined surface under gravity (see Fig. 15). The goal is to investigate and demonstrate the effects of the dynamic wall mobility, not only on the moving contact lines as observed in the previous subsection with the bouncing water drop problem, but also on the overall motion of the water drop and especially its speed.

Fig. 15 shows the problem configuration. We consider two parallel solid walls $\overline{AB}$ and $\overline{CD}$, inclined at a certain angle (inclination angle) with respect to the horizontal direction. The flow domain formed by the two walls is rectangular, with $\overline{AB} = 12.5\ mm$ and

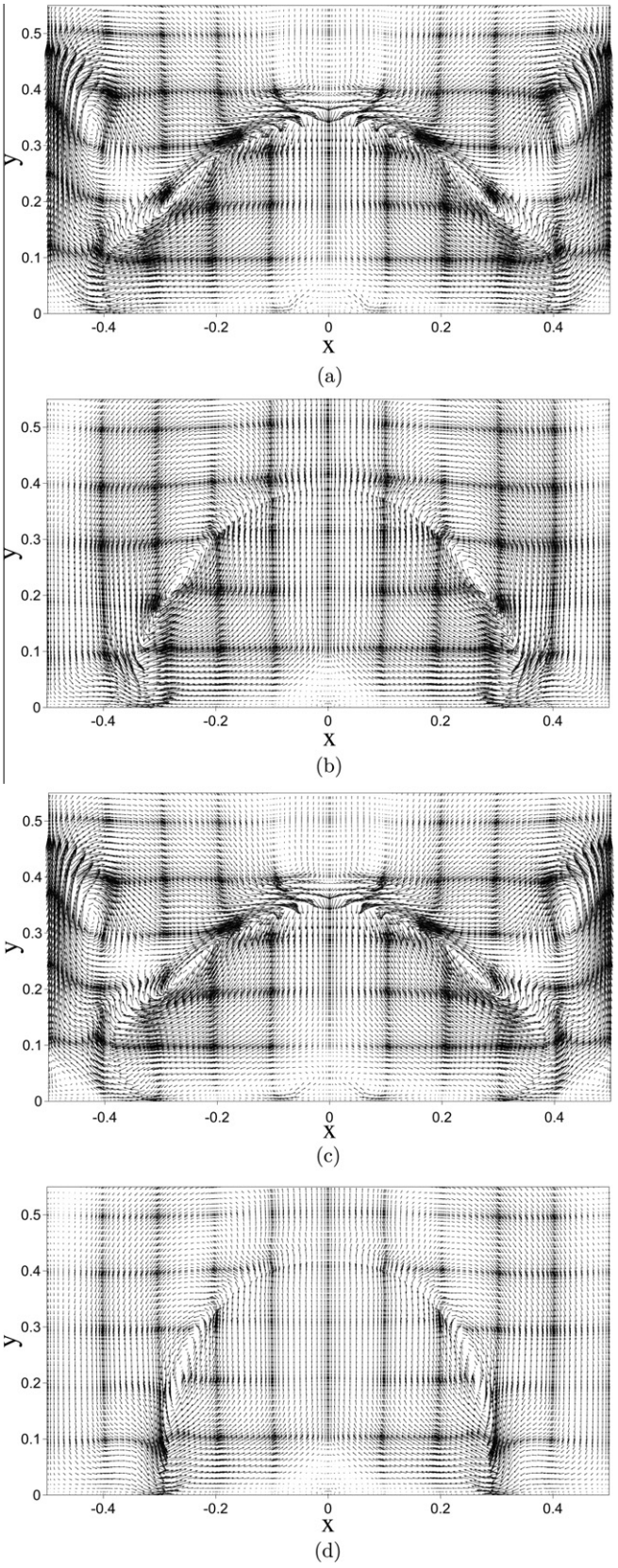

Fig. 14. Velocity field patterns with different dynamic wall mobility (static contact angle 120°): snapshots at two time instants: $t = 0.45$ ((a) and (c)) and $t = 0.6125$ ((b) and (d)). (a) and (b), $D_w^* = 0.0$; (c) and (d), $D_w^* = 0.2$. Plots (a) and (c) here respectively correspond to the air–water interfacial profiles in Figs. 13(a) and 13(c); plots (b) and (d) here correspond to Figs. 13(e) and 13(g).

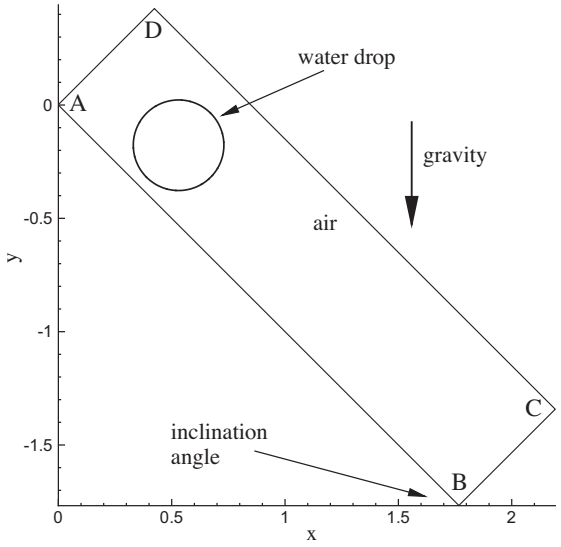

Fig. 15. Problem configuration for a water drop moving down a slope.

$\overline{AD} = 3\ mm$. The corner A is located at the origin of the coordinate system. We assume periodic boundary conditions at the inlet $\overline{AD}$ and the outlet $\overline{BC}$ to mimic an infinitely long inclined channel. The gravity is assumed to be in the $-y$ direction. A circular water drop of diameter 2 mm, surrounded by air, is initially at rest inside the channel, with its center located 1.25 mm away from the lower wall $\overline{AB}$ and 2.5 mm from the inlet $\overline{AD}$. The water drop is released at $t = 0$, falls onto the lower wall, and starts moving down the slope. The problem is to simulate the motion of the water drop in this process. The physical parameters for the problem and the procedure for flow variable normalization are the same as in the previous subsections, with characteristic length $L = 5$ mm and characteristic velocity $U_0 = \sqrt{g_0 L}$ (where $g_0 = 1\ \mathrm{m/s^2}$); see (40) and (37).

To simulate the problem, we discretize the domain with 150 equal-sized quadrilateral elements (25 elements in wall-parallel direction, and 6 elements in wall-normal direction). We employ an element order 14 for all elements in the simulations. On the lower and upper walls, no slip conditions have been used for the velocity, and the dynamic contact-angle boundary conditions (7a) and (7b) are imposed for the phase field function. At the inlet/outlet $\overline{AD}$ and $\overline{BC}$, periodic boundary conditions have been used for all flow variables. For the initial conditions, we use a zero velocity, and an initial phase field function given by (44). We have considered two inclination angles for the channel walls: 30° and 60°. The static contact angle is fixed at 90° throughout the simulations, and the dynamic wall mobility D_w^* is varied systematically.

We first compare motions of the water drop with and without the dynamic wall mobility D_w. Fig. 16 shows a temporal sequence of snapshots of the water drop (contour level $\phi = 0$) without dynamic wall mobility ($D_w^* = 0$), for a slope inclination angle 30°. The water drop occupies the shaded (or colored) regions in the plots, and note that the upper wall of the channel is not shown. Upon release, the water drop falls and attaches onto the inclined lower wall (slope in the figure), forming moving contact lines (Fig. 16(a)–(b)). The water drop undergoes a dramatic change in shape (Fig. 16(b)–(g)). While the drop moves down the slope, its shape oscillates about the center of mass, alternately spreading and shrinking along the wall-parallel and wall-normal directions (Figs. 16(d)–(m)). Over time, the shape oscillation attenuates and gradually disappears. The water drop assumes a shape reminiscent of a semi-ellipse, and exhibits an overall motion down the slope (Figs. 16(n)–(p)).

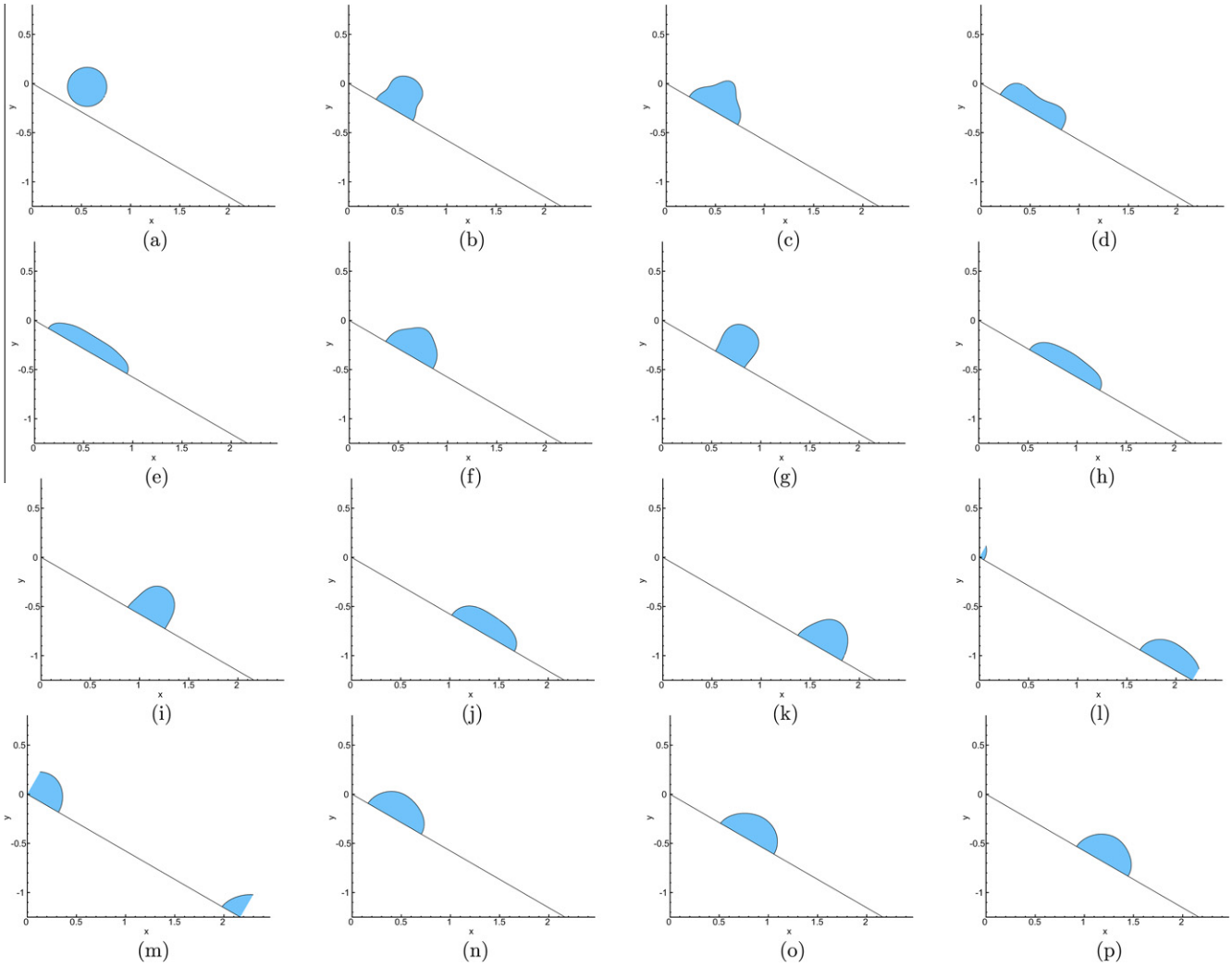

Fig. 16. Temporal sequence of snapshots of water drop moving down a slope (inclination angle 30°, static contact angle 90°, $D_w^* = 0$): (a) $t = 0.0125$, (b) $t = 0.1375$, (c) $t = 0.1625$, (d) $t = 0.2$, (e) $t = 0.2375$, (f) $t = 0.325$, (g) $t = 0.3875$, (h) $t = 0.5125$, (i) $t = 0.6375$, (j) $t = 0.7625$, (k) $t = 0.8875$, (l) $t = 1.0125$, (m) $t = 1.1375$, (n) $t = 1.2625$, (o) $t = 1.3875$, (p) $t = 1.5125$. Upper channel wall is not shown.

For comparison, we demonstrate in Fig. 17 the behavior of the water drop in the presence of dynamic wall mobility, with $D_w^* = 0.2$. Compared to the case with no dynamic wall mobility, the prominent difference is that here the oscillation about the center of mass rapidly dies down and the water drop largely exhibits only a down-slope motion. The water drop quickly reaches a "terminal" shape, which resembles a semi-circle but is asymmetric about the leading and trailing sides. One can also observe that the instantaneous contact angles deviate from the static contact angle (90^0) notably; see e.g. Fig. 17(c).

In Fig. 18 we compare the long-time profiles of the air–water interface with and without the effect of dynamic wall mobility, for slope inclination angles 30° (top row) and 60° (bottom row). The static contact angle is 90° in all cases. We observe a notable effect of the dynamic wall mobility on the long-time shape of the water drop. Without dynamic wall mobility ($D_w^* = 0$), the water drop appears more elongated in the wall-parallel direction (Figures 18(a) and (c)). Although in this case the drop shape also exhibits asymmetry about the leading and trailing sides, the contact angles at the leading/trailing contact lines both take the static contact angle value. On the other hand, with dynamic wall mobility ($D_w^* = 0.2$), the profile of the water drop resembles more closely a semi-circle with an asymmetry (Figs. 18(b)–(d)), and the advancing and receding contact angles deviate notably from the static contact angle (90°).

We also observe that the dynamic wall mobility affects significantly the speed of the water drop moving down the slope. This is demonstrated in Fig. 19 with the center of mass of the water drop as a function of time, obtained for a slope inclination angle 60° and different D_w^* values. Plot (a) is for the x coordinate and plot (b) is for the y coordinate. At $t \lesssim 0.13$, the curves with different D_w^* values overlap with one another, which corresponds to the initial free fall of the water drop onto the slope. The time period $0.13 \lesssim t \lesssim 0.3$ approximately corresponds to the impact of the water drop on the slope. Without dynamic wall mobility ($D_w^* = 0$), the impact causes a severe deformation and induces a large spread of the water drop along the wall-parallel direction (see Fig. 16e). The dynamic wall mobility reduces the deformation and the drop spread along the slope. As D_w^* increases, the deformation due to the impact becomes considerably less significant when compared to $D_w^* = 0$. These characteristics are responsible for the differences in the x coordinates during $0.13 \lesssim t \lesssim 0.3$ in Fig. 19(a). After this initial time period ($t \gtrsim 0.3$), one can observe a distinct effect of the D_w^* values on the motion of the water drop. The drop speed (in both x and y directions), which corresponds to the magnitude of the slope in the curves, shows a strong dependence on the dynamic

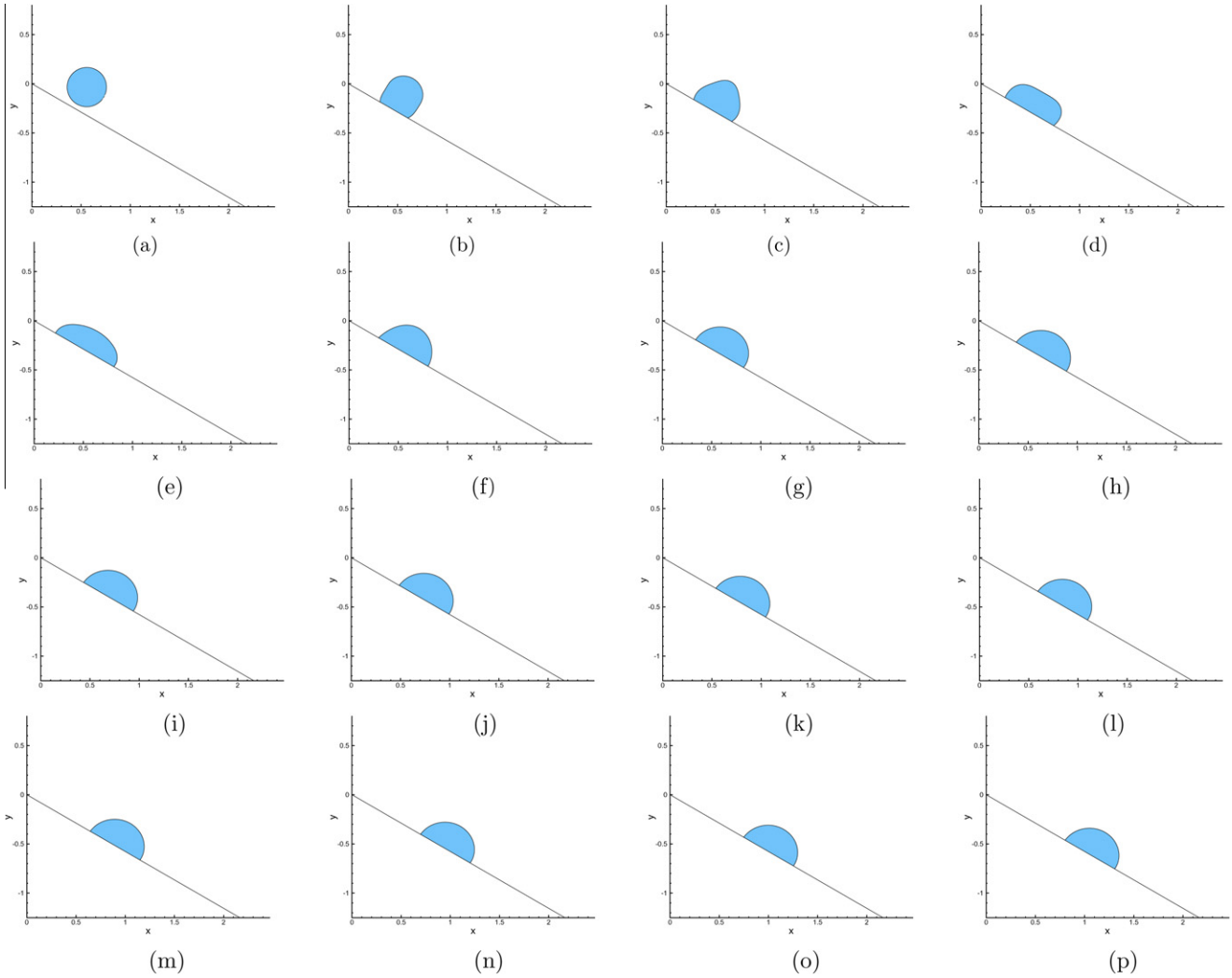

Fig. 17. Temporal sequence of snapshots of water drop moving down a slope (inclination angle 30°, static contact angle 90°, $D_w^* = 0.2$): (a) $t = 0.0125$, (b) $t = 0.1375$, (c) $t = 0.1625$, (d) $t = 0.2$, (e) $t = 0.2375$, (f) $t = 0.325$, (g) $t = 0.3875$, (h) $t = 0.5125$, (i) $t = 0.6375$, (j) $t = 0.7625$, (k) $t = 0.8875$, (l) $t = 1.0125$, (m) $t = 1.1375$, (n) $t = 1.2625$, (o) $t = 1.3875$, (p) $t = 1.5125$.

wall mobility D_w^*. The slope magnitude of the curves decreases as D_w^* increases, indicating that the water drop moves slower down the slope with a larger D_w^*. Zero dynamic wall mobility results in the fastest down-slope motion.

4. Concluding remarks

In this paper we have presented an efficient scheme for imposing the dynamic contact angle boundary conditions for the phase field approach. The scheme results in only *de-coupled* equations after discretization.

First, we have developed an algorithm for imposing the dynamic contact angle boundary conditions to the Cahn–Hilliard equation. Our strategy consists of two components: (1) we first ignore the boundary conditions and transform the Cahn–Hilliard equation into two *nominally de-coupled* Helmholtz type equations; (2) then we treat the dynamic contact angle boundary conditions in such a manner that the two Helmholtz type equations are *truly de-coupled*. To solve the Cahn–Hilliard equation, together with the dynamic contact angle boundary conditions, our overall algorithm therefore results in two *de-coupled* Helmholtz type equations after discretization. The formulation is provided in a form suitable for spectral element (and also finite element) type spatial discretizations.

Then, we combine the above algorithm, together with a scheme for variable-density Navier–Stokes equations we developed in [12], to form an efficient method for the coupled system of Navier–Stokes and Cahn–Hilliard equations involving large density ratios. The resultant method can deal with contact line problems under dynamic and also static contact angle boundary conditions. The method is endowed with several features that make it very efficient:

- Computations for all flow variables (phase field function, velocity, pressure) are completely *de-coupled*.
- Only *constant* and *time-independent* coefficient matrices are involved in the resulting linear algebraic system for all flow variables, even though the Navier–Stokes/Cahn–Hilliard coupled system involves variable density and variable viscosity fields. The coefficient matrices can be pre-computed during pre-processing.
- Only *de-coupled* Helmholtz type (including Poisson) equations need to be solved for each flow variable.

Moreover, the method is suitable for dealing with large density ratios, which has been demonstrated by ample numerical simulations.

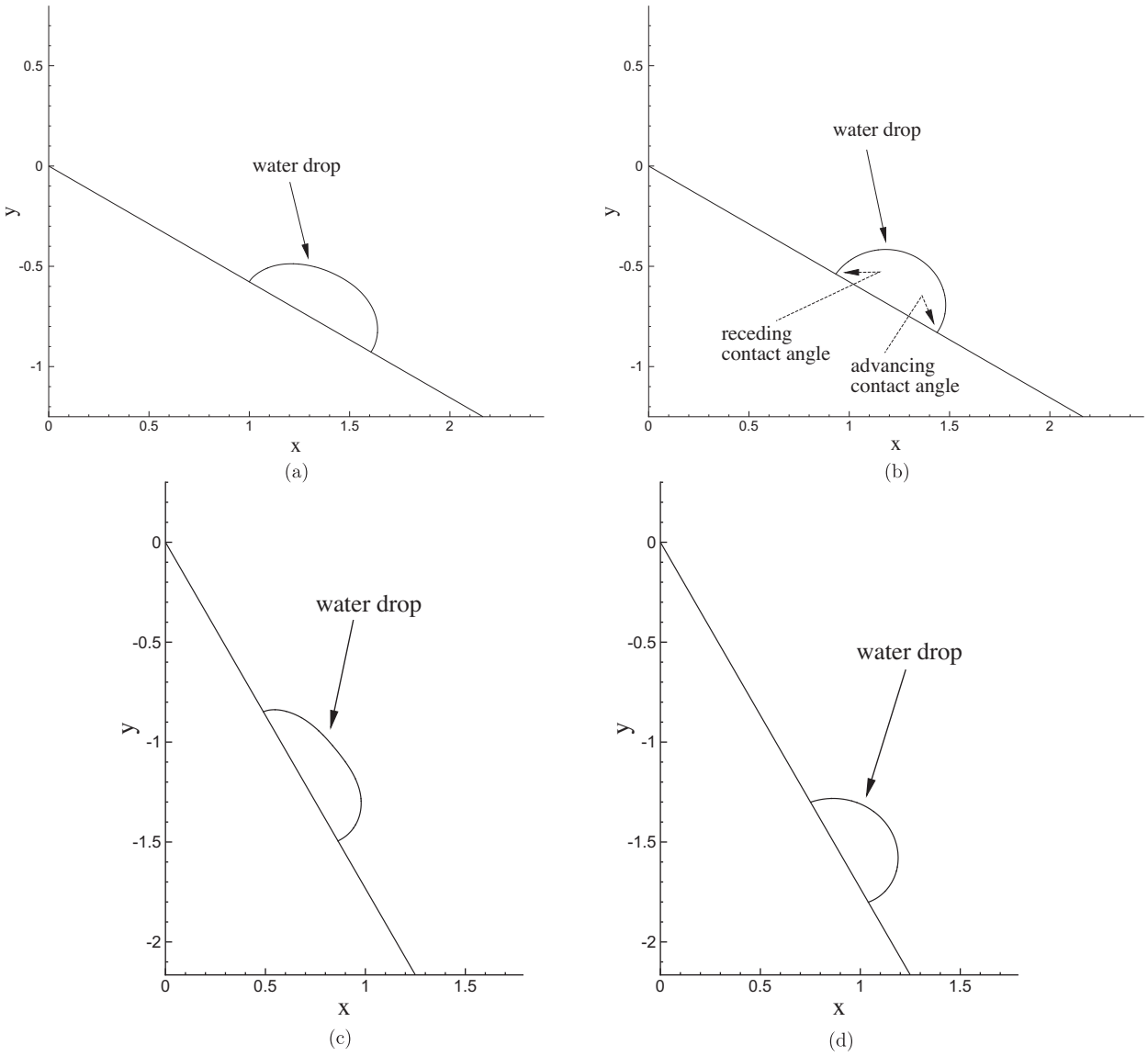

Fig. 18. Comparison of profiles of air–water interface over long time (static contact angle 90°): (a) and (b), slope inclination angle 30°; (c) and (d), slope inclination angle 60°; (a) and (c), $D_w^* = 0.0$; (b) and (d), $D_w^* = 0.2$.

Our numerical tests with air–water two-phase flows show that the dynamic wall mobility parameter (D_w) strongly affects the contact line dynamics and the profiles of the air–water interface. The prominent effect of dynamic wall mobility appears to retard the contact line motion, and to cause the advancing/receding contact angles to deviate from the static contact angle. This effect becomes stronger as the value of dynamic wall mobility increases.

The dynamic contact angle boundary condition as given by Eq. (4) can reasonably account for the contact angle hysteresis (deviation between instantaneous and equilibrium contact angles) due to the dynamic effects such as contact line motion. However, in its current form (with constant θ_s), it does not account for the hysteresis of the static contact angle, as observed in e.g. a pendant water drop resting on an inclined slope. The related issues will be deferred to further studies in the future.

Let us finally comment on the stability of the time-stepping scheme employed in the current paper. Due to its semi-implicit nature, the current scheme is only conditionally stable, and the time step size Δt is restricted by a maximum time step size. A rigorous stability analysis of the overall scheme is quite difficult. Here we briefly mention the main factors in the scheme that induce the restrictions on the time step size:

- The explicit treatment of the convective terms, $\mathbf{u}\cdot\nabla\mathbf{u}$ in the Navier–Stokes equation and $\mathbf{u}\cdot\nabla\phi$ in the Cahn–Hilliard equation. This will impose a CFL condition on the time step size.
- The explicit treatment of the nonlinear term $h(\phi)$ in the Cahn–Hilliard equation (5c). This will also induce a restriction on Δt. However, under certain assumption about the form of $h(\phi)$ (i.e. existence of an upper bound for $|h'(\phi)|$), if the chosen constant S (Eq. (8)) is sufficiently large, it can be proved that the first-order scheme for the Cahn–Hilliard equation (excluding convective term) is un-conditionally stable with the explicit treatment of $h(\phi)$; see [33].
- The explicit treatment of $\mathbf{D}(\mathbf{u}) = (\nabla\mathbf{u} + \nabla\mathbf{u}^T)$ in the term $\nabla\mu\cdot\mathbf{D}(\mathbf{u})$ in the Navier–Stokes equation (48). This induces a CFL-like constraint on the time step size [2], where $\nabla\mu = \frac{1}{2}(\mu_1 - \mu_2)\nabla\phi$ plays the role of a "convection velocity".

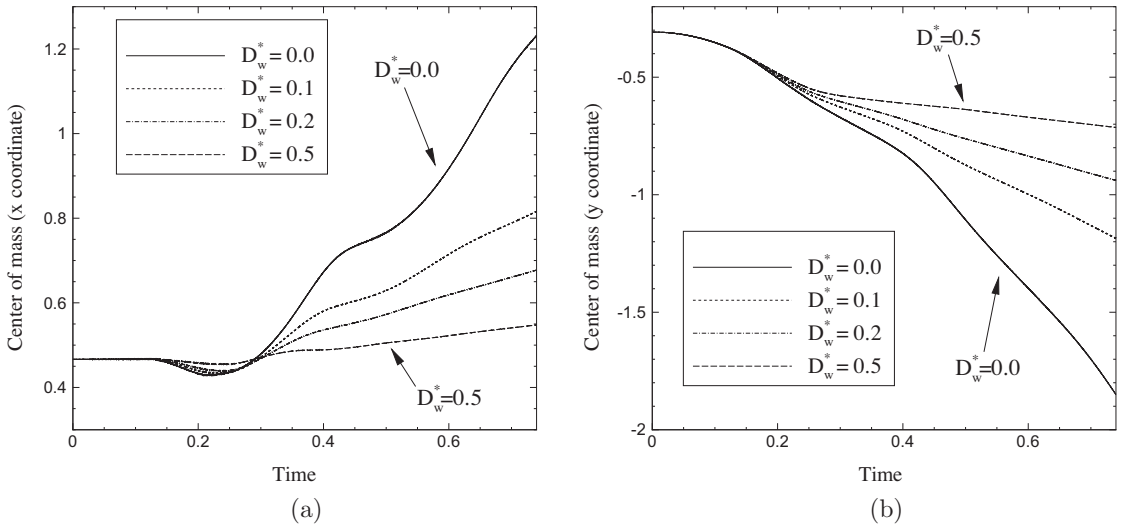

Fig. 19. Time histories of the water-drop center of mass, (a) x coordinate, and (b) y coordinate, for slope inclination angle 60°.

- The explicit treatment of the pressure P in the corrective pressure term $\left(\frac{1}{\rho_0}-\frac{1}{\rho}\right)\nabla P$ in Eq. (49a).

In addition, the following numerical treatments of the dynamic contact angle boundary conditions also contribute to the restrictions on the maximum allowable time step size:

- The explicit treatment of $\frac{\partial\phi}{\partial t}$ in (28) when imposing dynamic contact angle condition for solving Eq. (26) for ψ.
- The explicit treatment of the nonlinear term $f_w'(\phi)$ when discretizing the contact angle conditions in (28) and (30).
- The explicit treatment of the convection term $\mathbf{u}\cdot\nabla\phi$ in (28) and (30).
- The explicit treatment of the nonlinear term $h(\phi)$ when discretizing the boundary condition for chemical potential in (24).

It is possible to devise fully implicit (monolithic) or linearly implicit schemes for the coupled Navier–Stokes/Cahn–Hilliard equations (see e.g. [33]). The benefit of these implicit schemes is that they can allow for larger time step sizes than the current scheme. However, such schemes result in linear algebraic systems coupling up different flow variables after discretization, and the linear systems involve variable (time-dependent) coefficient matrices due to the variable density and variable dynamic viscosity. As noted in [12], the time-dependent nature requires the recomputation of the coefficient matrices every time step. The associated cost is very significant, and it grows rapidly as the problem size increases. Furthermore, Newton-type iterations are also involved at the outer level for solving nonlinear algebraic equations in the case of fully implicit schemes. Compared with these costly operations involved in such methods, the scheme in the current paper (and in [12]) completely de-couples the computations for different flow variables, and for each variable it involves only constant coefficient matrices which can be pre-computed. Furthermore, the current scheme only involves the solution of several separate Helmholtz type (including Poisson) equations within a time step. Due to these characteristics, the current scheme is extremely fast compared to the fully/linearly implicit schemes. Moreover, for many situations the maximum time step size that can be used in simulations is dictated by accuracy rather than stability. In addition, for certain problems more detailed dynamics of the two-phase system is of interest, which will require smaller time step sizes in numerical simulations. These situations also favor the current scheme.

Acknowledgements

The author gratefully acknowledges the support from ONR and NSF. Computer time was provided by XSEDE through an XRAC grant.

Appendix A. A scheme for variable-density Navier–Stokes equations

This appendix summarizes the formulation of a scheme we developed in [12] for the variable-density Navier–Stokes equations, (5a), (5b), with the following boundary condition:

$$\mathbf{u}|_{\partial\Omega}=\mathbf{w}(\mathbf{x},t), \tag{47}$$

where $\mathbf{w}(\mathbf{x},t)$ is the prescribed velocity on the domain boundary $\partial\Omega$.

We first transform the Navier–Stokes Eq. (5a) into an equivalent but slightly different form,

$$\rho\left(\frac{\partial\mathbf{u}}{\partial t}+\mathbf{u}\cdot\nabla\mathbf{u}\right)=-\nabla P+\mu\nabla^2\mathbf{u}+\nabla\mu\cdot(\nabla\mathbf{u}+\nabla\mathbf{u}^T)-\lambda(\nabla^2\phi)\nabla\phi+\mathbf{f}(\mathbf{x},t), \tag{48}$$

where $P=p+\frac{\lambda}{2}\nabla\phi\cdot\nabla\phi$ is an effective pressure, and will also be loosely called pressure. Note that the variable density ρ and viscosity μ are given by (6). The phase field function ϕ, and if necessary $\nabla^2\phi$, are assumed to be known.

We consider how to solve the system of (48) and (5b), together with the boundary condition (47). The formulation of the scheme is summarized below. Given $(\mathbf{u}^n,P^n)$, we successively solve for the pressure, and the velocity as follows:

For pressure P^{n+1}

$$\frac{\gamma_0\tilde{\mathbf{u}}^{n+1}-\hat{\mathbf{u}}}{\Delta t}+\frac{1}{\rho_0}\nabla P^{n+1}=-\mathbf{N}(\mathbf{u}^n)+\left(\frac{1}{\rho_0}-\frac{1}{\rho^{n+1}}\right)\nabla P^n-\frac{\mu^{n+1}}{\rho^{n+1}}\nabla\times\nabla\times\mathbf{u}^n+\frac{1}{\rho^{n+1}}\nabla\mu^{n+1}\cdot\mathbf{D}(\mathbf{u}^n)-\frac{\lambda}{\rho^{n+1}}\nabla^2\phi^{n+1}\nabla\phi^{n+1}+\frac{1}{\rho^{n+1}}\mathbf{f}^{n+1}, \tag{49a}$$

$$\nabla\cdot\tilde{\mathbf{u}}^{n+1}=0, \tag{49b}$$

$$\mathbf{n}\cdot\tilde{\mathbf{u}}^{n+1}|_{\partial\Omega}=\mathbf{n}\cdot\mathbf{w}^{n+1}. \tag{49c}$$

For velocity $\mathbf{u}^{n+1}$

$$\frac{\gamma_0\mathbf{u}^{n+1}-\gamma_0\tilde{\mathbf{u}}^{n+1}}{\Delta t}-\nu_m\nabla^2\mathbf{u}^{n+1}=-\mathbf{N}(\mathbf{u}^{*,n+1})+\mathbf{N}(\mathbf{u}^n)+\nu_m\nabla\times\nabla\times\mathbf{u}^{*,n+1}+\left(\frac{1}{\rho_0}-\frac{1}{\rho^{n+1}}\right)\nabla(P^{n+1}-P^n)-\frac{\mu^{n+1}}{\rho^{n+1}}\nabla\times\nabla\times(\mathbf{u}^{*,n+1}-\mathbf{u}^n)+\frac{1}{\rho^{n+1}}\nabla\mu^{n+1}\cdot\left[\mathbf{D}(\mathbf{u}^{*,n+1})-\mathbf{D}(\mathbf{u}^n)\right], \tag{50a}$$

$$\mathbf{u}^{n+1}|_{\partial\Omega}=\mathbf{w}^{n+1}. \tag{50b}$$

In the above equations, $\tilde{\mathbf{u}}^{n+1}$ is an intermediate velocity, an approximation of $\mathbf{u}^{n+1}$. $\mathbf{N}(\mathbf{u})=\mathbf{u}\cdot\nabla\mathbf{u}$, and $\mathbf{D}(\mathbf{u})=\nabla\mathbf{u}+\nabla\mathbf{u}^T$. If χ denotes a generic variable, $\hat{\chi}$ and $\chi^{*,n+1}$ have the same meanings as those defined in Section 2.1. ρ^{n+1} and μ^{n+1} are respectively the density and dynamic viscosity at time step $(n+1)$, determined from Eq. (6) based on ϕ^{n+1}. The constant ρ_0 is given by $\rho_0=\min(\rho_1,\rho_2)$. The parameter ν_m is a chosen constant satisfying $\nu_m\geqslant\frac{1}{2}\frac{\max(\mu_1,\mu_2)}{\min(\rho_1,\rho_2)}$. ϕ^{n+1} and $\nabla^2\phi^{n+1}$ are assumed to be known.

The feature of the scheme that allows for a constant (time-independent) coefficient matrix for the pressure is the term $\frac{1}{\rho_0}\nabla P^{n+1}$ in (49a), and also the correction terms, $(\frac{1}{\rho_0}-\frac{1}{\rho^{n+1}})\nabla P^n$ in (49a) and $(\frac{1}{\rho_0}-\frac{1}{\rho^{n+1}})\nabla(P^{n+1}-P^n)$ in (50a). The feature that allows for a constant coefficient matrix for the velocity is the term $\nu_m\nabla^2\mathbf{u}^{n+1}$ in Eq. (50a), and its explicit counterpart in "rotational form" $\nu_m\nabla\times\nabla\times\mathbf{u}^{*,n+1}$. We note that this strategy for dealing with a diffusion term with a variable diffusion coefficient was discussed in [16] (section 9, page 114), and was also used by other researchers (e.g. [2,32]). One can also recognize that the above procedures for computing the pressure P^{n+1} and the velocity $\mathbf{u}^{n+1}$ overall represent a velocity correction type strategy (see [17,11]).

To implement the above scheme, we take the L^2-inner product of Eq. (49a) with ∇q, and we obtain the following Poisson equation in the weak form for P^{n+1},

$$\int_\Omega\nabla P^{n+1}\cdot\nabla q=\rho_0\int_\Omega\left[\mathbf{G}+\nabla\left(\frac{\mu^{n+1}}{\rho^{n+1}}\right)\times\boldsymbol{\omega}^n\right]\cdot\nabla q-\rho_0\int_{\partial\Omega}\frac{\mu^{n+1}}{\rho^{n+1}}\mathbf{n}\times\boldsymbol{\omega}^n\cdot\nabla q-\frac{\gamma_0\rho_0}{\Delta t}\int_{\partial\Omega}\mathbf{n}\cdot\mathbf{w}^{n+1}q,\quad\forall q\in H^1(\Omega), \tag{51}$$

where

$$\mathbf{G}=\frac{1}{\rho^{n+1}}\left[\mathbf{f}^{n+1}-\lambda\nabla^2\phi^{n+1}\nabla\phi^{n+1}+\nabla\mu^{n+1}\cdot\mathbf{D}(\mathbf{u}^n)\right]+\frac{\hat{\mathbf{u}}}{\Delta t}-\mathbf{N}(\mathbf{u}^n)+\left(\frac{1}{\rho_0}-\frac{1}{\rho^{n+1}}\right)\nabla P^n \tag{52}$$

and $\boldsymbol{\omega}=\nabla\times\mathbf{u}$ denotes the vorticity, and we have used Eqs. (49b) and (49c). Take the L^2-inner product of Eq. (50a) with scalar test function φ, and note that the intermediate velocity can be substituted by, based on Eq. (49a),

$$\frac{\gamma_0}{\Delta t}\tilde{\mathbf{u}}^{n+1}=\mathbf{G}-\frac{\mu^{n+1}}{\rho^{n+1}}\nabla\times\boldsymbol{\omega}^n-\frac{1}{\rho_0}\nabla P^{n+1}.$$

We then obtain the weak form of (50a) for $\mathbf{u}^{n+1}$:

$$\frac{\gamma_0}{\nu_m\Delta t}\int_\Omega\varphi\mathbf{u}^{n+1}+\int_\Omega\nabla\varphi\cdot\nabla\mathbf{u}^{n+1}=\frac{1}{\nu_m}\int_\Omega\left[\mathbf{R}+\nabla\left(\frac{\mu^{n+1}}{\rho^{n+1}}\right)\times\boldsymbol{\omega}^{*,n+1}\right]\varphi-\frac{1}{\nu_m}\int_\Omega\left(\frac{\mu^{n+1}}{\rho^{n+1}}-\nu_m\right)\boldsymbol{\omega}^{*,n+1}\times\nabla\varphi-\frac{1}{\nu_m}\int_{\partial\Omega}\left(\frac{\mu^{n+1}}{\rho^{n+1}}-\nu_m\right)\mathbf{n}\times\boldsymbol{\omega}^{*,n+1}\varphi,\quad\forall\varphi\in H_0^1(\Omega), \tag{53}$$

where $H_0^1(\Omega)=\left\{v\in H^1(\Omega):\ v|_{\partial\Omega}=0\right\}$, and

$$\mathbf{R}=\frac{1}{\rho^{n+1}}\left[\mathbf{f}^{n+1}-\lambda\nabla^2\phi^{n+1}\nabla\phi^{n+1}+\nabla\mu^{n+1}\cdot\mathbf{D}(\mathbf{u}^{*,n+1})\right]+\frac{\hat{\mathbf{u}}}{\Delta t}-\mathbf{N}(\mathbf{u}^{*,n+1})-\frac{1}{\rho^{n+1}}\nabla P^{n+1}. \tag{54}$$

The weak forms (51) and (53) can be directly employed in spatial discretizations with C^0 spectral elements (or finite elements). We assume that $\nabla^2\phi^{n+1}$ in (52) and (54) are already known, which for example can be computed based on Eq. (23b) with $\nabla^2\phi^{n+1}=\psi^{n+1}-\alpha\phi^{n+1}$.

The final algorithm consists of solving (51) for P^{n+1}, and then solving (53) for $\mathbf{u}^{n+1}$. Note that only *constant* coefficient matrices are involved in these equations, which can be pre-computed during pre-processing, even though variable density and variable viscosity are involved in the original Navier–Stokes equation. One can also observe that the intermediate velocity $\tilde{\mathbf{u}}^{n+1}$ in the original formulation of the scheme is eliminated from the re-formulated algorithm, (51) and (53), and that it is never actually computed in the implementation.

References

[1] S. Afkhami, S. Zaleski, M. Bussmann, A mesh-dependent model for applying dynamic contact angles to VOF simulations, J. Comput. Phys. 228 (2009) 5370–5389.
[2] V.E. Badalassi, H.D. Ceniceros, S. Banerjee, Computation of multiphase systems with phase field models, J. Comput. Phys. 190 (2003) 371–397.
[3] A. Carlson, M. Do-Quang, G. Amberg, Dissipation in rapid dynamic wetting, J. Fluid Mech. 682 (2011).
[4] A. Carlson, M. Do-Quang, G. Amberg, Modeling of dynamic wetting far from equilibrium, Phys. Fluids 21 (2011) 121701.
[5] R.G. Cox, The dynamics of the spreading of liquids on a solid surface. part i. viscous flow, J. Fluid Mech. 168 (1986) 169–194.
[6] P.G. de Gennes, Capillarity and Wetting Phenomena, Springer, 2004.
[7] P.G. de Genns, Wetting: statics and dynamics, Rev. Mod. Phys. 57 (1985) 827–863.
[8] H. Ding, P.D.M. Spelt, Inertial effects in droplet spreading: a comparison between diffuse-interface and level-set simulations, J. Fluid Mech. 576 (2007) 287–296.
[9] S. Dong, BDF-like methods for nonlinear dynamic analysis, J. Comput. Phys. 229 (2010) 3019–3045.
[10] S. Dong, G.E. Karniadakis, A. Ekmekci, D. Rockwell, A combined DNS-PIV study of the turbulent near wake, J. Fluid Mech. 569 (2006) 185–207.
[11] S. Dong, J. Shen, An unconditionally stable rotational velocity-correction scheme for incompressible flows, J. Comput. Phys. 229 (2010) 7013–7029.
[12] S. Dong, J. Shen, A time-stepping scheme involving constant coefficient matrices for phase field simulations of two-phase incompressible flows with large density ratios, J. Comput. Phys. 231 (2012) 5788–5804.
[13] J.-B. Dupont, D. Legendre, Numerical simulation of static and sliding drop with contact angle hysteresis, J. Comput. Phys. 229 (2010) 2453–2478.
[14] E.B. Dussan, S.H. Davis, On the motion of fluid-fluid interface along a solid surface, J. Fluid Mech. 65 (1974) 71–95.
[15] P. Gao, J.J. Feng, A numerical investigation of the propulsion of water walkers, J. Fluid Mech. 668 (2011) 363–383.
[16] D. Gottlieb, S.A. Orszag, Numerical Analysis of Spectral Methods: Theory and Applications, SIAM, CMBS, 1977.
[17] J.L. Guermond, J. Shen, Velocity-correction projection methods for incompressible flows, SIAM J. Numer. Anal. 41 (2003) 112–134.
[18] L.M. Hocking, A moving fluid interface. Part 2. the removal of the force singularity by a slip flow, J. Fluid Mech. 79 (1977) 209–229.
[19] L.M. Hocking, Rival contact-angle models and the spreading of drops, J. Fluid Mech. 239 (1992) 671–681.
[20] C. Huh, L.E. Scriven, Hydrodynamic model of steady movement of a solid/liquid/fluid contact line, J. Colloid Interface Sci. 35 (1971) 85–101.

[21] D. Jacqmin, Contact-line dynamics of a diffuse fluid interface, J. Fluid Mech. 402 (2000) 57–88.
[22] G.E. Karniadakis and S.J. Sherwin. Spectral/hp element methods for computational fluid dynamics, 2nd edn. Oxford University Press, 2005.
[23] H.G. Lee, J. Kim, Accurate contact angle boundary conditions for the Cahn–Hilliard equations, Comput. Fluids 44 (2011) 178–186.
[24] C. Liu, J. Shen, A phase field model for the mixture of two incompressible fluids and its approximation by a fourier-spectral method, Physica D 179 (2003) 211–228.
[25] J. Lowengrub, L. Truskinovsky, Quasi-incompressible Cahn–Hilliard fluids and topological transitions, Proc. R. Soc. London A 454 (1998) 2617–2654.
[26] S. Manservisi, R. Scardovelli, A variational approach to the contact angle dynamics of spreading droplets, Comput. Fluids 38 (2009) 406–424.
[27] S.J. Osher, J.A. Sethian, Fronts propagating with curvature dependent speed: algorithms based on Hamilton–Jacobi formulations, J. Comput. Phys. 79 (1988) 12–49.
[28] T. Qian, X.-P. Wang, P. Sheng, A variational approach to moving contact line hydrodynamics, J. Fluid Mech. 564 (2006) 333–360.
[29] D. Richard, D. Quere, Bouncing water drops, Europhys. Lett. 50 (2000) 769–775.
[30] R. Scardovelli, S. Zaleski, Direct numerical simulation of free-surface and interfacial flow, Ann. Rev. Fluid Mech. 31 (1999) 567–603.
[31] J.A. Sethian, P. Semereka, Level set methods for fluid interfaces, Ann. Rev. Fluid Mech. 35 (2003) 341–372.
[32] J. Shen, X. Yang, An efficient moving mesh spectral method for the phase-field model of two-phase flows, J. Comput. Phys. 228 (2009) 2978–2992.
[33] J. Shen, X. Yang, Energy stable schemes for Cahn–Hilliard phase-field model of two-phase incompressible flows, Chin. Ann. Math. Ser. B 31 (2010) 743–758.
[34] P.D. Spelt, A level-set approach for simulations of flows with multiple moving contact lines with hysteresis, J. Comput. Phys. 207 (2005) 389–404.
[35] G. Tryggvason, B. Bunner, A. Esmaeeli, et al., A front-tracking method for computations of multiphase flow, J. Comput. Phys. 169 (2001) 708–759.
[36] S.O. Unverdi, G. Tryggvason, A front-tracking method for viscous, incompressible, multi-fluid flows, J. Comput. Phys. 100 (1992) 25–37.
[37] A.L. Yarin, Drop impact dynamics: splashing, spreading, receding, bouncing . . ., Ann. Rev. Fluid Mech. 38 (2006) 159–192.
[38] P. Yue, J.J. Feng, Wall energy relaxation in the Cahn–Hilliard model for moving contact lines, Phys. Fluids 23 (2011) 012106.
[39] P. Yue, J.J. Feng, C. Liu, J. Shen, A diffuse-interface method for simulating two-phase flows of complex fluids, J. Fluid Mech. 515 (2004) 293–317.
[40] P. Yue, C. Zhou, J.J. Feng, Spontaneous shrinkage of drops and mass conservation in phase-field simulations, J. Comput. Phys. 223 (2007) 1–9.
[41] P. Yue, C. Zhou, J.J. Feng, Sharp-interface limit of the Cahn–Hilliard model for moving contact lines, J. Fluid Mech. 645 (2010) 279–294.
[42] P. Yue, C. Zhou, J.J. Feng, C.F. Ollivier-Gooch, H.H. Hu, Phase-field simulations of interfacial dynamics in viscoelastic fluids using finite elements with adaptive meshing, J. Comput. Phys. 291 (2006) 47–67.
[43] X. Zheng, S. Dong, An eigen-based high-order expansion basis for structured spectral elements, J. Comput. Phys. 230 (2011) 8573–8602.
[44] C. Zhou, P. Yue, J.J. Feng, C.F. Ollivier-Gooch, H.H. Hu, 3D phase-field simulations of interfacial dynamics in newtonian and viscoelastic fluids, J. Comput. Phys. 229 (2010) 498–511.